

Electronic Controlled Vertical Integration Directional Coupler Design with Artificial Neural Networks for Dual Band Application

Master's THESIS

Department of Electrical and Electronics in Engineering

by

Hacer DANACI

ORCID 0000-0003-4057-4749

Thesis Advisor: Assoc. Prof. Dr. Merih PALANDÖKEN

September, 2021

This is to certify that we have read the thesis **Electronic Controlled Vertical Integration Directional Coupler Design with Artificial Neural Networks for Dual Band Application** submitted by **Hacer DANACI**, and it has been judged to be successful, in scope and in quality, at the defense exam and accepted by our jury as a MASTER'S THESIS.

APPROVED BY:

Advisor: **Assoc. Prof. Dr. Merih PALANDÖKEN**
İzmir Kâtip Çelebi University

Committee Members:

Assoc. Prof. Dr. Merih PALANDÖKEN
İzmir Kâtip Çelebi University

Assist. Prof. Dr. Esra Aycan BEYAZIT
İzmir Kâtip Çelebi University

Assist. Prof. Dr. Şule ÇOLAK
Adana Alparslan Türkeş Bilim ve Teknoloji University

Date of Defense: 06.08.2021

Declaration of Authorship

I, **Hacer DANACI**, declare that this thesis titled **Electronic Controlled Vertical Integration Directional Coupler Design with Artificial Neural Networks for Dual Band Application** and the work presented in it are my own. I confirm that:

- This work was done wholly or mainly while in candidature for the Master's / Doctoral degree at this university.
- Where any part of this thesis has previously been submitted for a degree or any other qualification at this university or any other institution, this has been clearly stated.
- Where I have consulted the published work of others, this is always clearly attributed.
- Where I have quoted from the work of others, the source is always given. This thesis is entirely my own work, with the exception of such quotations.
- I have acknowledged all major sources of assistance.
- Where the thesis is based on work done by myself jointly with others, I have made clear exactly what was done by others and what I have contributed myself.

Signature:

Date: 06.09.2021

Electronic Controlled Vertical Integration Directional Coupler Design with Artificial Neural Networks for Dual Band Application

Abstract

In this thesis, two different varactor diode-based electronically controllable planar directional couplers with DC biasing control circuits are presented. The magnitude values of reverse bias voltages of varactor diodes have been controlled through one microcontroller via Bluetooth wireless communication by the mobile application. Any coupling ratio of the proposed smart directional coupler to be set at the operating frequency can be widely tuned by training the experimental data in a machine learning algorithm for the determination of the correct voltage to be applied in the DC biasing network. The operating frequency band of the proposed coupler is extending from 500 MHz up to 1 GHz covering and 2 GHz up to 3 GHz the dedicated wide/local area IoT (internet of things) frequency bands ranging from radio frequency identification (RFID) up to mobile network applications. The proposed directional couplers prototypes have been fabricated on low loss Rogers RO4003C substrate. The high isolation level of more than 32 dB and low return loss higher than 10 dB have been experimentally measured in the whole operating frequency band. The numerical and experimental results of the proposed directional coupler agree well. The compact directional coupler has the high technical potential to be used for smart IoT applications.

Keywords: Electronically tunable coupler, Raspberry Pi 3B+, size reduction, Bluetooth controller, power dividing ratio, Machine Learning.

Dual Band Uygulaması için Yapay Sinir Ağları ile Elektronik Kontrollü Dikey Entegrasyon Yönlü Bağlayıcı Tasarımı

ÖZ

Bu tezde, iki farklı varaktör diyot tabanlı, elektronik olarak kontrol edilebilen, DC öngerilim kontrol devrelerine sahip düzlemsel yönlü kuplörler sunulmuştur. Varaktör diyotların ters öngerilim gerilimlerinin büyüklük değerleri, mobil uygulama ile Bluetooth kablosuz iletişim üzerinden tek bir mikrodenetleyici üzerinden kontrol edilmiştir. Önerilen akıllı yönlü kuplörün çalışma frekansına ayarlanması için herhangi bir bağlantı oranı, DC kutuplamalı ağda uygulanacak doğru voltajın belirlenmesi için deneysel veriler makine öğrenme algoritmasında eğitilerek geniş çapta ayarlanabilir. Önerilen kuplörün çalışma frekans bandı, radyo frekansı tanımlamadan (RFID) mobil ağ uygulamalarına kadar geniş/yerel alan IoT (nesnelerin internet) frekans bantlarını kapsayan 500 MHz'den 1 GHz'e kadar ve 2 GHz'den 3 GHz'e kadar uzanmaktadır. Önerilen yönlü kuplör prototipi, düşük kayıplı Rogers RO4003C substratı üzerinde üretilmiştir. 32 dB'den fazla yüksek izolasyon seviyesi ve 10 dB'den yüksek düşük geri dönüş kaybı, tüm çalışma frekans bandında deneysel olarak ölçülmüştür. Önerilen yönlü kuplörün sayısal ve deneysel sonuçları büyük ölçüde uyumludur. Kompakt yönlü kuplör, akıllı IoT uygulamaları için kullanılmak üzere yüksek teknik potansiyele sahiptir.

Anahtar Kelimeler: Elektronik olarak ayarlanabilen kuplör, Raspberry Pi 3B+, boyut küçültme, Bluetooth denetleyici, güç bölme oranı, Makine Öğrenimi.

To my family

Acknowledgment

This thesis would not have been possible without the support of my advisor Assoc. Prof. Dr. Merih PALANDÖKEN. I would like to thank for his guidance and support throughout the masters degree study. It is an honor for me to work with him and benefit from his vast knowledge. Whenever I needed something throughout the study, his door was open for me.

Table of Contents

Declaration of Authorship.....	ii
Abstract.....	iii
Öz	iv
Acknowledgment	vi
List of Figures	ix
List of Tables.....	ix
List of Abbreviations.....	xiv
1 Introduction	1
2 Directional Coupler Theory	7
2.1 Theoretical Background of the Directional Coupler.....	7
2.2 S-Parameter of the Directional Coupler	8
2.3 Coupled Line Directional Couplers	10
2.4 The 90° Hybrid Couplers.....	13
2.5 The 180° Hybrid Couplers.....	13
3 Design and Numerical Calculation Results of the Electronically Controllable Directional Couplers	15
3.1 Design and Numerical Calculation Results of the Coupler Design I	15
3.2 Design and Numerical Calculation Results of the Coupler Design II	21
4 Fabrication and Measurement Results of the Electronically Controllable Directional Couplers	28
4.1 Fabrication and Measurement Results of the Coupler Design I.....	28
4.2 Fabrication and Measurement Results of the Coupler Design II.....	32
5 Machine Learning Algorithm for Smart and Remotely Controllable Directional Couplers	36

5.1	Collection of Data for Smart Coupler Designs	37
5.2	Selection of Machine Learning Algorithm for Coupler Design I	39
5.3	Implementation of Machine Learning Algorithm for Coupler Design I	41
5.4	Selection of Machine Learning Algorithm for Coupler Design II	42
5.5	Implementation of Machine Learning Algorithm for Coupler Design II	43
6	Integration of the Electronically Controllable Smart Coupler System.....	45
6.1	Android Interface Designs	45
6.1.1	Android Interface Design for Coupler Design I.....	45
6.1.2	Android Interface Design for Coupler Design II.....	47
6.2	DC Supply.....	48
6.3	System Integration and Working Principle.....	49
7	Conclusion.....	53
	References	55
	Appendices	61
	Appendix A Varactor Diode Value	62
	Appendix B Validation of Regression Machine Learning Problem	63
	Appendix C Amplifier Schematics	65
	Curriculum Vitae	68

List of Figures

Figure 1. 1: The block diagram of smart directional coupler system.....	4
Figure 2.1: Symbols for directional couplers that are commonly used.....	7
Figure 2.2: Diverse coupled transmission line geometries. (a) Coupled stripline. (b) Coupled stripline. (c) Coupled microstrip lines [39]	10
Figure 2.3: A three-wire coupled line equivalent capacitance network [39]	11
Figure 2.4: Even- and odd mode excitations for a coupled line, and the resulting equivalent capacitance networks. (a) Even-mode excitation. (b) Odd-mode excitation [39]	11
Figure 2.5: Geometry of a hybrid coupler.....	13
Figure 2.6: Symbol for a 180° hybrid junction.	14
Figure 3.1: Layout of the Coupler Design I	16
Figure 3.2: The circuit model of the Coupler Design I.....	16
Figure 3.3: Reflection coefficient value by changing DC block capacitor value	18
Figure 3.4: S-Parameter comparison of the Coupler Design I without varactor diode	18
Figure 3.5: S-Parameters results of the Coupler Design I by biasing reverse voltage at 900 MHz	19
Figure 3.6: The reflection coefficient values of the Coupler Design I with different varactor voltage feeding	19

Figure 3.7: Insertion losses of the Coupler Design I with different varactor voltage feeding.....	20
Figure 3.8: Coupling coefficient value of the Coupler Design I with different varactor voltage feeding	20
Figure 3.9: S41 numerical calculation results the Coupler Design I with different varactor voltage feeding.....	21
Figure 3.10: Layout of the Coupler Design II.....	21
Figure 3.11: Top layer of the Coupler Design II.....	22
Figure 3.12: Ground plane layer of the Coupler Design II	22
Figure 3.13: Resonator layer of the Coupler Design II.....	23
Figure 3.14: S-Parameter value of the directional coupler without resonator	24
Figure 3.15: S-Parameter value of the vertical integration directional coupler without varactor diode.....	24
Figure 3.16: Reflection coefficient values of the Coupler Design II.....	25
Figure 3.17: S-Parameters results of the Coupler Design II by biasing reverse voltage at 2.45 GHz	25
Figure 3.18: Reflection coefficient values of the Coupler Design II with different varactor voltage feeding.....	26
Figure 3.19: Insertion loss values of the Coupler Design II with different varactor voltage feeding	26
Figure 3.20: The Coupling values of the Coupler Design II with different varactor voltage feeding	27
Figure 3.21: The Isolation loss values of the Coupler Design II with different varactor voltage feeding	27
Figure 4.1: Fabricated Coupler Design I.....	28

Figure 4.2: Block diagram of the experimental setup for reflection coefficient result	29
Figure 4.3: The comparison of simulated and measured reflection coefficient value of the Coupler Design I	29
Figure 4.4: Block diagram of the experimental setup for the S21, S31, and S41 S-Parameter results.....	30
Figure 4.5: The experimental setup for the S21, S31, and S41 S-Parameter results .	30
Figure 4.6: The comparison of simulated and measured reflection coefficient value of the Coupler Design II.....	31
Figure 4.7: The comparison of simulated and measured coupling value of the Coupler Design I.....	31
Figure 4.8: The comparison of simulated and measured reflection isolation loss of the Coupler Design I.....	31
Figure 4.9: Fabricated Coupler Design II	32
Figure 4.10: Block diagram of the experimental setup of the Coupler Design II for S11 S-Parameter results	32
Figure 4.11: The experimental setup for the S11 S-Parameter results.....	33
Figure 4.12: Block Diagram of the Experimental Setup of the Vertical Integration Directional Coupler S31 S-Parameter results	33
Figure 4.13: The experimental setup for the S21, S31, and S41 S-Parameter results	34
Figure 4.14: The comparison of simulated and measured reflection coefficient value of the Coupler Design II.....	34
Figure 4.15: The comparison of simulated and measured insertion loss value of the Coupler Design II.....	35

Figure 4.16: The comparison of simulated and measured coupling value of the Coupler Design II.....	35
Figure 4.17: The comparison of simulated and measured isolation loss of the Coupler Design II.....	35
Figure 5.1: ML model of the smart coupler systems	37
Figure 5.2: Block diagram of the measurement system for S21	37
Figure 5. 3: Block diagram of the measurement system for S31	38
Figure 5. 4: The sample of the prediction curve for 880,900, and 920 MHz: a) $ S_{21} $ and b) $ S_{31} $	42
Figure 5. 5: The sample of the prediction curve for 2400 MHz, 2450 MHz, and 2500 MHz	44
Figure 6.1: Android interface outline design for a system of the Coupler Design I..	46
Figure 6.2: Android interface outline design for a system of the Coupler Design II.	47
Figure 6.3: Amplifier design (a), Fabricated amplifier (b)	48
Figure 6.4: Electronically controllable system design for first directional coupler...	49
Figure 6.5: The system integration and validation setup for the S21, S31	49
Figure 6.6: Electronically controllable system design for vertical integration directional coupler.....	50
Figure 6.7: The system integration and validation setup of the Coupler Design II for the S31 and Volt.....	50
Figure 6.8: Flowchart diagram of the Coupler Design I application side.....	51
Figure 6.9: Flowchart diagram of the Coupler Design I Raspberry Pi 3 B+ side	51
Figure 6.10: Flowchart diagram of the Coupler Design II application side.....	52
Figure 6.11: Flowchart diagram of the Coupler Design II Raspberry Pi Pico.....	52

List of Tables

Table 1.1: Samples of tunable directional coupler models in the literature.....	5
Table 3.1: Geometrical parameter of numerical the Coupler Design I structure with dimension	17
Table 3.2: Geometrical Parameters of Electronically Controllable Directional Coupler Structure and Optimized Dimensions from Numerical Calculations Performed at 2.45 GHz	23
Table 5.1: 900 MHz applications dataset.....	38
Table 5.2: 2.45 GHz applications dataset.....	39
Table 5.3: Regression algorithm performance comparison for S21 output value.....	39
Table 5.4: Regression algorithm performance comparison for S31 output value.....	40
Table 5.5: Constant of third degree polynomial regression equation for Coupler Design I	41
Table 5.6: Regression algorithm performance comparison for output value.....	43
Table 5.7: Constant of third degree polynomial regression equation for Coupler Design II.....	44
Table 7.1: Comparison of RF performance parameters between the proposed coupler structure and referenced coupler	54

List of Abbreviations

APP	Application
CMOS	Complementary Metal Oxide Semiconductor
FDTD	Finite Difference Time Domain
IDE	Integrated Development Environment
IoT	Internet of Things
MEMS	Micro Electro Mechanical System
MIT	Massachusetts Institute of Technology
ML	Machine Learning
PCB	Printed Circuit Board
PDR	Power Division Ratio
RF	Radio Frequency
TEM	Transverse Electro-Magnetic

Chapter 1

Introduction

In microwave and radio-frequency (RF) systems, directional couplers commonly have been utilized for the versatile purpose to distribute input power into different output ports with the necessary coupling ratio levels.

With the rise of the Internet of Things (IoT), the ability of user-based reconfigurable individual RF components in wireless systems have become increasingly important. Bluetooth module-controlled wireless hardware, which is easy and reaches inexpensive, supports user-based interface approaches.

There are different technological approaches including Micro Electro Mechanical System (MEMS)[1,2], Complementary Metal Oxide Semiconductor (CMOS) [3-5]. Printed Circuit Board (PCB) [6-12], Coaxial Line [13-15], Waveguide [16,17], for directional coupler design and fabrication.

In addition to different technological approaches, various techniques have been used to include the tunable feature in RF components. Examples of these techniques are mechanically, electrically, photonic-based to ensure reconfigurable printed RF components [18-24].

H. A. Affel of A.T.T., Co. is widely credited with inventing the first directional coupler, with his U.S. Patent 1615896, which was filed in 1922 and granted in 1927. In the 1940s, the MIT Radiation Laboratory invented and characterized a wide range of waveguide couplers, including multihole couplers, the Bethe hole coupler, and the Schwinger coupler [25]. The directional coupler was a useful tool for laboratory and production testing at this time[26]. Later, many waveguide couplers were fabricated [16, 27].

A group at Stanford Research Institute designed coupled TEM line directional couplers in the 1950s, primarily using stripline transmission line structures [28]. Then there were microstrip couplers, which were planar and open-sided, making it easy to mount semiconductors and other devices [29, 30].

In 1999, the first varactor-tuned electronically tunable directional coupler was proposed. To control the resonance condition of a parallel LC resonator, the bias voltage of the varactor is varied [31].

Among the versatile different technological and technical approaches, the PCB technology and electronically tunable technic have been extensively addressed to ensure the cost efficiency in the fabricated components [22–24].

Wang and others, a novel coupler structure based on two varactors was realized to create an electronically tunable microstrip parallel coupler. A tunable coupling coefficient can be obtained by adjusting the capacitances of the two varactors. After entering the required coupling coefficient into the computer, the computer automatically controls the data acquisition component (DAQ) NI USB-6008 to output a pair of outputs [32].

Zhang and others proposed a flexible quadrature coupler. Its control voltages provided tunability for simultaneous operating frequency, coupling ratio, and coupling-direction control with three varactor diodes. A tunable operating frequency of 1 to 1.5 GHz, a controllable power division ratio between output ports of 1 to 0.7, and a switchable operational direction of forwarding and backward were demonstrated for the coupler [6].

Chi and others presented a simple and clear varactor-tuned balanced directional coupler structure. The power dividing ratio of the coupler is specifically tuned by a single control biasing voltage across only two shunt varactors and depends on the available capacitance tuning ratio. Power dividing ratio can be tuned range from -5.5 dB to -11.9 dB at 1 GHz operating frequency where the differential-mode insertion loss is better than 0.84 dB in terms of input power efficiency, the differential-mode isolation and return loss greater than 23.2 dB and 27.5 dB, respectively [7].

Chu and others presented a novel tunable directional coupler design with a very wide adjusting range of coupling ratios. The proposed tunable directional coupler was fabricated and tested using microstrip technology at 2.4 GHz. The experimental representation features the widest coupling ratio tuning range ($-39\sim 29$ dB) among the literature with an insertion loss of 1.2 dB and excellent port isolation greater than 22 dB [23].

Tan and Lin designed two different frequency reconfigurable rat-race couplers with power-dividing ratios of 1:1 and 2:1, the tuning elements are three varactor diodes. The operating frequencies of the proposed couplers with power division ratios of 1:1 and 2:1 are adjusted range from 840 MHz to 2480 MHz and 840 MHz to 2410 MHz, respectively, with return loss and isolation of better than 15 dB [8].

Tianyu and Wenquan proposed a microstrip coupler model with reconfigurable coupling and frequency. In the study three varactor diodes were used to ensure tunability. Tunable frequency range from 1 to 3 GHz with 3 dB coupling, and a tunable coupling coefficient range from 0.86 to 9.5 dB at operating frequency (2GHz) [10].

Shen and others proposed coupled line coupler with a reconfigurable coupling ratio and center frequency simultaneously. In this study, the tunability on coupler performance parameters has been accomplished through eight varactor diodes placed in the coupler branches. Power division ratio can be electronically adjusted from 3 dB to 0.71 9 dB for the operating frequencies between 0.55GHz and 1.48 GHz division ratio can be varied from 0 dB to 9 dB at 1 GHz [11].

Some tunable directional coupler models in the literature, fabrication technology, and tuning elements of the couplers have been given in Table 1.1.

In this thesis, two different user-based and electronically controllable planar directional couplers are designed, fabricated, and measured for IoT applications. Figure 1.1 presents a block diagram of the directional coupler system connected to a microcontroller to reverse bias the varactor diode through an Android-based RF component-specific application in a remote system.

The design and numerical calculation of the directional couplers have been carried out via the CST Microwave Studio software. The directional couplers have been fabricated

by using the MITS Eleven Lab brand PCB device in İzmir Kâtip Çelebi University. The couplers have been fabricated on Rogers 4003 substrate having a loss tangent of 0.001, dielectric constant of 3.55 and height of 1.52 mm. The varactor diode has been selected from Skyworks Solutions Inc. (SVM2019) for two designs.

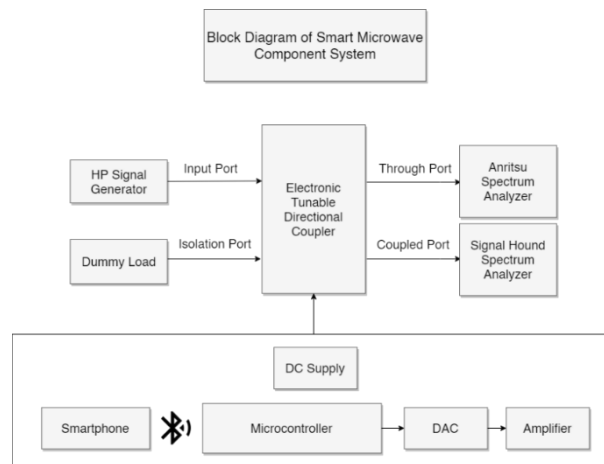


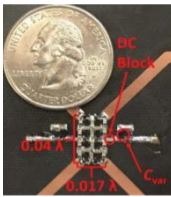
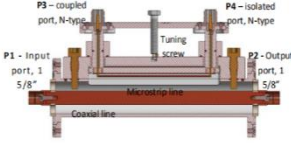
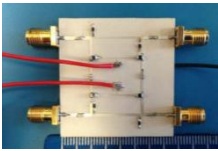
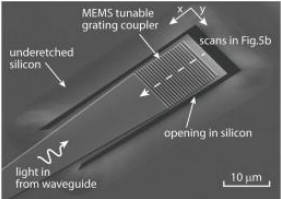
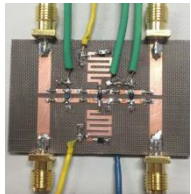
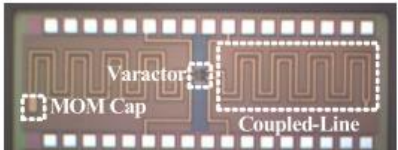

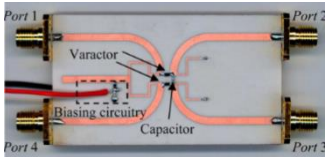
Figure 1. 1: The block diagram of smart directional coupler system

Varactor diode has been used to ensure the electronic tunability of the coupling of the proposed smart directional coupler. The capacitance values of the varactor diode have been remotely set through the Bluetooth-controlled biasing network. For two different systems, two different android interfaces have been designed.

First, the user-based reconfigurable directional coupler is composed of three-layer as ground, substrate, and directional coupler. The coupler including only one varactor diode whose biasing network is Bluetooth-controlled via a Raspberry Pi 3 B+ microcontroller for the setting of desired coupling performance through machine learning algorithms. The control unit of the directional coupler dedicated to being used for DC biasing of varactor diode result in the user operating the proposed directional coupler at the desired frequency with the intended coupling coefficient.

The second user-based reconfigurable directional coupler is composed of six-layer from the bottom layer ground, substrate, space, resonator structure which provide tunability via varactor diode, substrate, and directional coupler structure respectively.

Table 1.1: Samples of tunable directional coupler models in the literature

Items	Geometry of the Coupler	Technology	Tuning Elements
[33]		PCB	Varactor
[18]		CW	Mechanically
[34]		PCB	Varactor
[35]		MEMS	Light
[36]		PCB	Varactor
[37]		CMOS	Varactor
[32]		PCB	Varactor
[38]		PCB	Varactor

The coupler has been named user-based tunable vertical integration directional coupler because it has six vertical layers. The coupler including only one varactor diode whose biasing network is Bluetooth-controlled via a Raspberry Pi Pico microcontroller for the setting of desired coupling performance through machine learning algorithms.

The control unit of the directional coupler dedicated to being used for DC biasing of varactor diode result in the user operating the proposed directional coupler at the desired frequency with the intended coupling coefficient.

This thesis study basically consists of seven chapter. In the introduction chapter, in addition to giving information to the general literature about the directional coupler, the couplers designed in the study are mentioned. In chapter II, the theoretical background of the directional coupler is explained in detail. Design and numerical calculation results of the electronically controllable directional couplers are presented in chapter III. In chapter IV, fabrication and measurement results of the electronically controllable directional couplers are represented. In chapter V, machine learning algorithms for smart and remotely controllable directional couplers are represented. In chapter VI, two different microcontroller-based smart control directional coupler systems are represented. The concluding remarks are conducted in chapter VII.

Chapter 2

Directional Coupler Theory

In this chapter, the theoretical background of the directional coupler is explained in detail.

2.1 Theoretical Background of the Directional Coupler

In order to understand how the directional coupler works, it is necessary to be able to analyze its theoretical background. Figure 2.1 describes the simple operation of a four-port coupler.

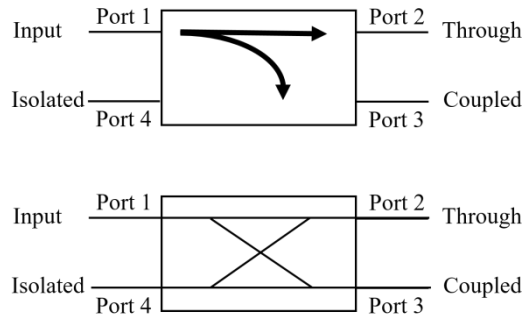


Figure 2.1: Symbols for directional couplers that are commonly used

When the input power is assumed to be applied to port 1, there are certain quantities used to define the characteristics of the directional coupler shown in from Equation 2.1a to Equation 2.1d.

$$\text{Coupling} = C = 10\log(P_1/P_3) = -20\log \beta \text{ dB} \quad (2.1a)$$

$$\text{Directivity} = D = 10\log(P_3/P_4) = -20\log(\beta/|S_{14}|) \text{ dB} \quad (2.1b)$$

$$\text{Isolation} = I = 10\log(P_1/P_4) = -20\log |S_{14}| \text{ dB} \quad (2.1c)$$

$$\text{Insertion Loss} = L = 10\log(P_1/P_2) = -20\log |S_{12}| \text{ dB} \quad (2.1d)$$

The *coupling* represents the percentage of input power that is coupled to port three. The *directivity* of a coupler indicates how well it isolates forward and backward waves. The *isolation* parameter specifies the percentage of power delivered to the uncoupled/isolated port. Finally, the insertion loss accounts for the amount of power delivered to the through port, which is reduced by the amount of power delivered to the coupled and isolated ports. The directivity and isolation of an ideal coupler are infinite [39].

2.2 S-Parameter of the Directional Coupler

The directional coupler's S-parameter matrix is defined as in Equation 2.2:

$$[S] = \begin{bmatrix} S_{11} & S_{12} & S_{13} & S_{14} \\ S_{21} & S_{22} & S_{23} & S_{24} \\ S_{31} & S_{32} & S_{33} & S_{34} \\ S_{41} & S_{42} & S_{43} & S_{44} \end{bmatrix} \quad (2.2)$$

The ideal symmetrical directional coupler should have a lossless scattering matrix. If the network is matched at every single port, then in the scattering matrix, all diagonal elements ($S_{ii} = 0$) become 0, as shown in Equation 2.3.

$$S_{11}=S_{22}=S_{33}=S_{44}=0 \quad (2.3)$$

In the reciprocal network, it has to be $S_{21}=S_{12}$, $S_{31}=S_{13}$, $S_{32}=S_{23}$, $S_{41}=S_{14}$, $S_{42}=S_{24}$, $S_{43}=S_{34}$.

The reciprocal and matched four-port network's S matrix has been given in Equation 2.4:

$$[S] = \begin{bmatrix} 0 & S_{12} & S_{13} & S_{14} \\ S_{12} & 0 & S_{23} & S_{24} \\ S_{13} & S_{23} & 0 & S_{34} \\ S_{14} & S_{24} & S_{34} & 0 \end{bmatrix} \quad (2.4)$$

In addition, there is no coupling between the input and isolation ports in an ideal directional coupler. So, Equation 2.5:

$$S_{14} = S_{41} = 0 \quad (2.5)$$

There is also no coupling between the coupled and through ports. So, Equation 2.6:

$$S_{23} = S_{32} = 0 \quad (2.6)$$

Then S matrix has been given in Equation 2.7 :

$$[S] = \begin{bmatrix} 0 & S_{12} & S_{13} & 0 \\ S_{12} & 0 & 0 & S_{24} \\ S_{13} & 0 & 0 & S_{34} \\ 0 & S_{24} & S_{34} & 0 \end{bmatrix} \quad (2.7)$$

The concept of unitary property implies that Equation 2.8,

$$[S] \cdot [S]^* = [I] \quad (2.8)$$

And, then the following formulation is reached as from Equation 2.9a to Equation 2.9d:

$$(|S_{12}|^2 + |S_{13}|^2) = 1 \quad (2.9a)$$

$$(|S_{12}|^2 + |S_{24}|^2) = 1 \quad (2.9b)$$

$$(|S_{13}|^2 + |S_{34}|^2) = 1 \quad (2.9c)$$

$$(|S_{24}|^2 + |S_{34}|^2) = 1 \quad (2.9d)$$

which imply that $|S_{13}|=|S_{24}|$ [using (2.9a) and (2.9b)], and that $|S_{12}|=|S_{34}|$ [using (2.9c) and (2.9d)].

2.3 Coupled Line Directional Couplers

Due to the interaction of electromagnetic fields between two unshielded transmission lines in close proximity, power can be coupled from one line to the other. Coupled transmission lines are such lines, and they generally have three conductors in close proximity, however additional conductors might be utilized. Figure 2.2 represents several samples of coupled transmission lines.

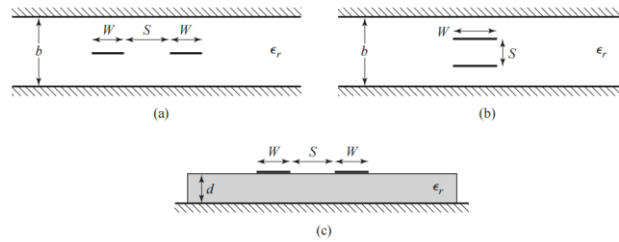


Figure 2.2: Diverse coupled transmission line geometries. (a) Coupled stripline. (b) Coupled stripline. (c) Coupled microstrip lines [39]

As shown in Figure 2.2 the coupled lines are symmetric, which the two conducting strips are the same width and location relative to the ground, which simplifies their operating analysis.

2.3.1 Coupled Line Theory

The coupled lines as shown in Figure 2.2 can be represented by the equivalent circuit shown in Figure 2.3. C12 indicates the capacitance between the two strip conductors, whereas C11 and C22 represent the capacitance between one strip conductor and ground, as shown in Figure 2.3.

It has to be $C_{11} = C_{22}$, because the strip conductors are the same size and position as the ground conductor.

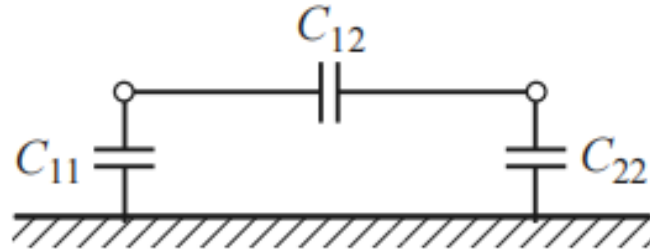


Figure 2.3: A three-wire coupled line equivalent capacitance network [39]

Consider two forms of coupled line excitations: the even mode, in which in the strip conductors, the currents are equal in amplitude and direction. And there's the odd mode when the currents in the strip conductors have the same amplitude but flow in opposite directions. Figure 2.4 depicts the electric field lines for these two situations.

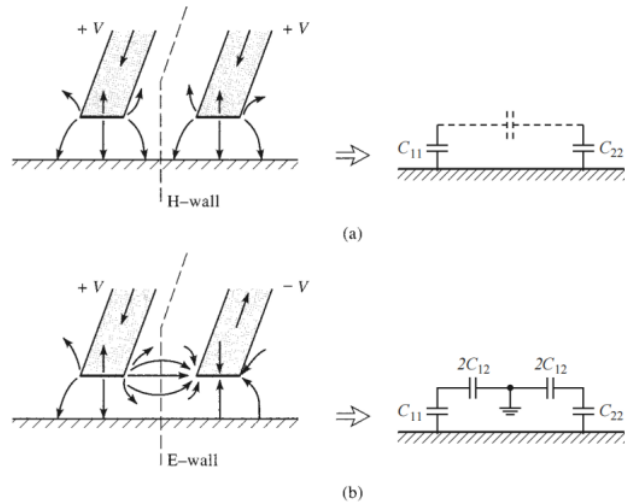


Figure 2.4: Even- and odd mode excitations for a coupled line, and the resulting equivalent capacitance networks. (a) Even-mode excitation. (b) Odd-mode excitation [39]

The propagation constant and phase velocity for both of these modes are the same since the line is TEM: $\beta = \omega/v_p$ and $v_p = c/\sqrt{\epsilon_r}$, where ϵ_r is the relative permittivity of the TEM line.

The electric field is symmetrical around the centerline in the even mode, and between the two strip conductors, no current flows. As a result, C_{12} is essentially open-circuited in the comparable circuit illustrated. For the even mode, the resultant capacitance of either line to ground is as in Equation 2.10:

$$C_e = C_{11} = C_{22} \quad (2.10)$$

Assume that the size and position of the two strip conductors are equal. Then for the even mode, the characteristic impedance is as in Equation 2.11:

$$Z_{0e} = \sqrt{\frac{L_e}{C_e}} = \frac{\sqrt{L_e C_e}}{C_e} = \frac{1}{v_p C_e} \quad (2.11)$$

On the line, the phase velocity of propagation is $v_p = \frac{c}{\sqrt{\epsilon_r}} = \frac{1}{\sqrt{L_e C_e}} = 1/\sqrt{L_o C_o}$.

The electric field lines for the odd mode have an odd symmetry about the centerline, and there is a voltage null between the two strip conductors. In this situation the effective capacitance between ground and strip conductor is as in Equation 2.12:

$$C_o = C_{11} + 2C_{12} = C_{22} + 2C_{12} \quad (2.12)$$

for the odd mode, the characteristic impedance is as in Equation 2.13:

$$Z_{0o} = \sqrt{\frac{L_o}{C_o}} = \frac{\sqrt{L_o C_o}}{C_o} = \frac{1}{v_p C_o} \quad (2.13)$$

The lines are assumed to be symmetric, and the fringing capacitances for even and odd modes are the same.

2.4 The 90° Hybrid Couplers

The hybrid couplers have equal power split with a 90° phase difference between through and coupled ports. This hybrid is commonly made in the form of a stripline or microstrip line, as shown in Figure 2.5.

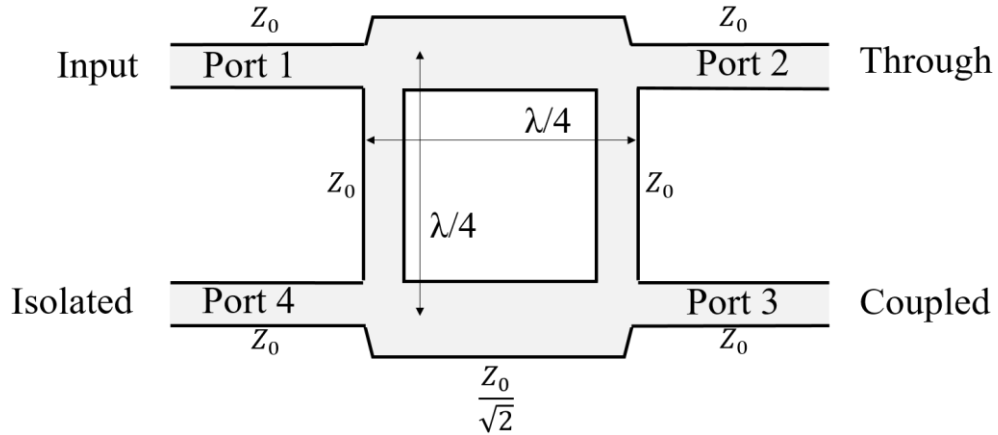


Figure 2.5: Geometry of a hybrid coupler

All ports matched, as shown in Figure 2.5. With a 90° phase shift between these outputs, power entering port 1 is evenly distributed between ports 2 and 3. Port 4 has no power connected to it (the isolated port). The scattering matrix has been given in Equation 2.14:

$$[S] = \frac{1}{\sqrt{2}} \begin{bmatrix} 0 & j & 1 & 0 \\ j & 0 & 0 & 1 \\ 1 & 0 & 0 & j \\ 0 & 1 & j & 0 \end{bmatrix} \quad (2.14)$$

Because each port can be utilized as an input port, the branch-line hybrid has a high degree of symmetry.

2.5 The 180° Hybrid Couplers

A four-port network with a 180° phase shift between the two output ports is known as a 180 hybrid junction. It may also be set up to produce outputs that are in phase. A signal supplied to port 1 will be equally divided into two in-phase components at ports

2 and 3, and port 4 will be isolated, as represented by the 180 hybrid symbol in Figure 2.6.

When the input is applied to port 4, it is evenly divided into two components with a 180 phase difference at ports 2 and 3, while port 1 is isolated. When used as a combiner with input signals at ports 2 and 3, the total of the inputs is generated at port 1, while the difference is formed at port 4.

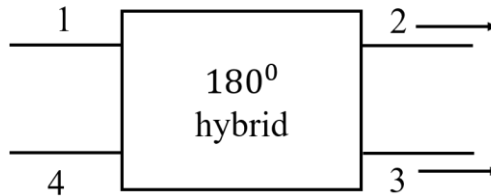


Figure 2.6: Symbol for a 180° hybrid junction.

As a result, ports 1 and 4 are known as the sum and difference ports, respectively. As a result, the scattering matrix has been given in Equation 2.15:

$$[S] = \frac{-j}{\sqrt{2}} \begin{bmatrix} 0 & 1 & 1 & 0 \\ 1 & 0 & 0 & -1 \\ 1 & 0 & 0 & 1 \\ 0 & -1 & 1 & 0 \end{bmatrix} \quad (2.15)$$

This matrix is unitary and symmetric, as the reader can see.

Chapter 3

Design and Numerical Calculation

Results of the Electronically

Controllable Directional Couplers

In this chapter, the design and numerical results of proposed coupler structures have been presented. In this thesis, two different electronically controllable directional coupler design concepts are realized for versatile applications and different operating frequencies. Electronically controllable directional coupler for 900 MHz applications is briefly referred to as Coupler Design I in the remainder of the thesis. An electronically controllable directional coupler for 2.45 GHz applications is briefly referred to as Coupler Design II in the remainder of the thesis. The design and numerical calculation of the directional couplers have been carried out using the CST Microwave Studio numerical analysis tool.

3.1 Design and Numerical Calculation Results of the Coupler Design I

The Coupler Design I structure has been planned to be created within the scope of the project consists of three layers as shown in Figure 3.1. These three layers consist of the metallic ground plane, dielectric material, and directional coupler structure from bottom to top respectively as shown in Figure 3.1. It has been planned to establish the electronic controllability required in the electronically controlled coupler design in the directional coupler structure.

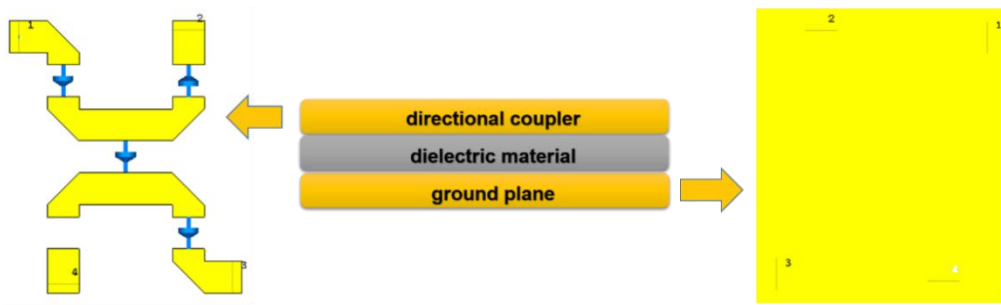


Figure 3.1: Layout of the Coupler Design I

The final configuration of the Coupler Design I geometry is shown in Figure 3.2, including the arrangement of varactors and DC bias networks. Table 3.1 lists the circuit characteristics and key physical dimensions. The loss tangent, dielectric constant, and height of the electronically tunable coupler are 0.001, 3.55, and 1.52 mm, respectively, on a Rogers Duroid 4003 substrate. The overall physical dimension of the proposed smart Coupler Design I is 13.66 mm x 15.99 mm x 1.59 mm, ($0.041 \lambda \times 0.048 \lambda \times 0,0047 \lambda$). λ is the guided wavelength at the 900 MHz operating frequency.

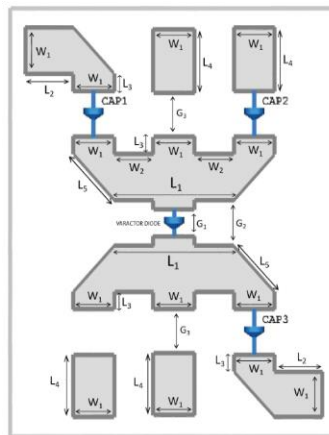


Figure 3.2: The circuit model of the Coupler Design I

Varactor diode has been selected from Skyworks Solutions Inc. (SVM2019). With reverse voltages ranging from 0 to 20 V, it has an adjustable capacitance range of 2.2 to 0.3 pF. See Appendix A for a varactor diode with changing reverse bias voltage value. Varactor diode is used to ensure the electronic tunability of the coupling

parameter of the proposed smart directional coupler. The capacitance values of the varactor diode have been remotely set through the Bluetooth-controlled biasing network. Three 20 pF SMD capacitors are incorporated within the coupler structure in order to protect the Network Vector Analyzer from possible DC supply.

Table 3.1: Geometrical parameter of numerical the Coupler Design I structure with dimension

Symbol	Value(mm)
L ₁	5
L ₂	2
L ₃	0.65
L ₄	2
L ₅	2.45
W ₁	1.71
W ₂	1.58
G ₁	1
G ₂	1.7
G ₃	1.65

Figure 3.3 shows return loss values with changing SMD capacitor values at varactor value 1pF. From Figure 3.3, it was observed that the frequency value decreased as the capacitor value increased. When the S parameter results with different varactor values were analyzed, 20 pF was chosen as the ideal value for 900 MHz applications.

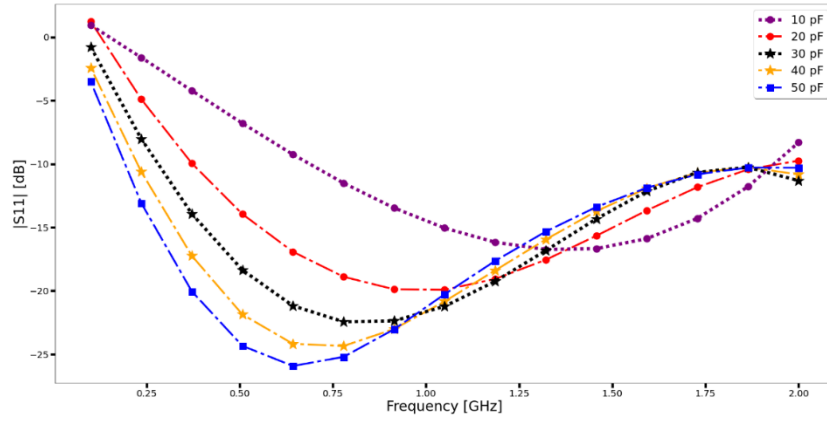


Figure 3.3: Reflection coefficient value by changing DC block capacitor value

Figure 3.4 depicts the S-Parameter Result of the Coupler Design I without varactor diode.

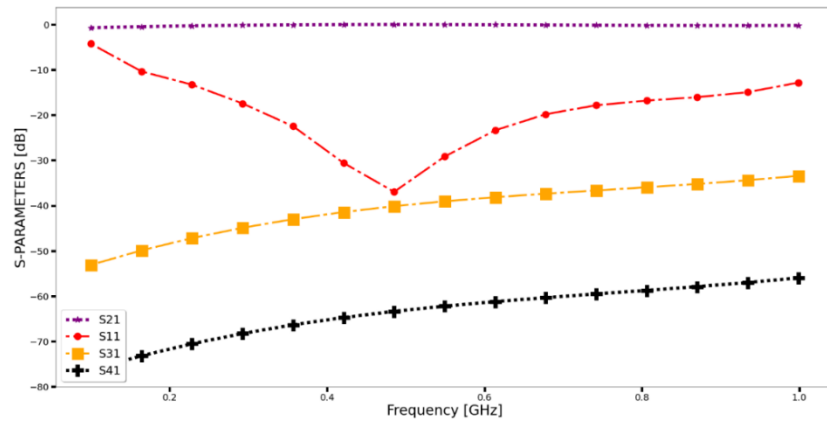


Figure 3.4: S-Parameter comparison of the Coupler Design I without varactor diode

At the operating frequency of 900 MHz, ideal return losses, insertion losses, and isolation losses are all realized, as shown in Figure 3.5 with the voltage changes between 0 and 20 V with a 1-volt difference. The designed coupler's return loss and isolation loss are both higher than 10 dB within the operational frequency spectrum. The simulated results of the designed directional coupler show a tuning coupling coefficient range from 4.51 and 19.37 dB at the operating frequency 900 MHz as shown in Figure 3.5.

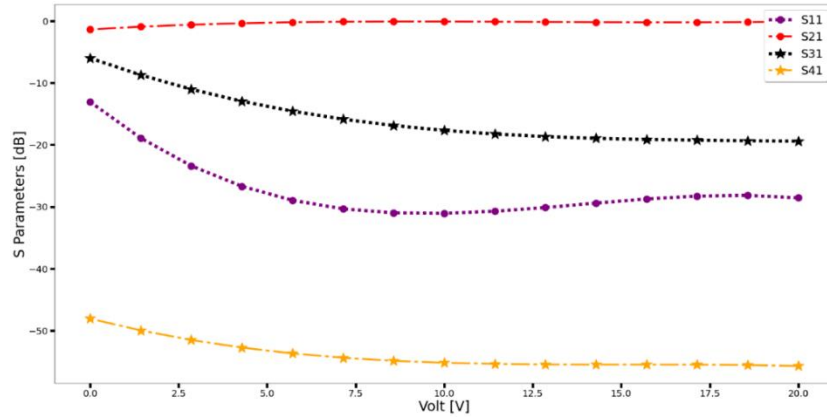


Figure 3.5: S-Parameters results of the Coupler Design I by biasing reverse voltage at 900 MHz

Figures 3.6, 3.7, 3.8, 3.9 show the numerical calculation results including return losses, insertion losses, coupling value, and isolation losses. Figure 3.6 represents return loss of Coupler Design I with different voltage values spans the 500 MHz to 1 GHz frequency range. The reflection coefficient ($|S_{11}|$) keeps higher than 13 dB at the entire frequency range.

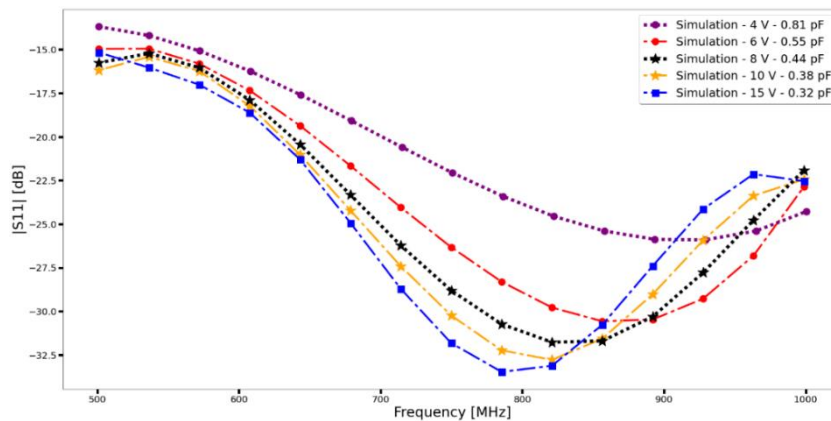


Figure 3.6: The reflection coefficient values of the Coupler Design I with different varactor voltage feeding

Figure 3.7 indicates insertion loss of the Coupler Design I with different volt-varactor values spans the 500 MHz to 1 GHz frequency range. The insertion losses ($|S_{21}|$) keep lower than 0.45 dB at the entire frequency range. Figure 3.8 shows the simulated coupling value of the Coupler Design I with versus reverse biasing voltages at the

frequency range from 500 MHz to 1 GHz. The simulated results of the designed directional coupler show a tuning coupling coefficient range from 500 MHz to 1 GHz.

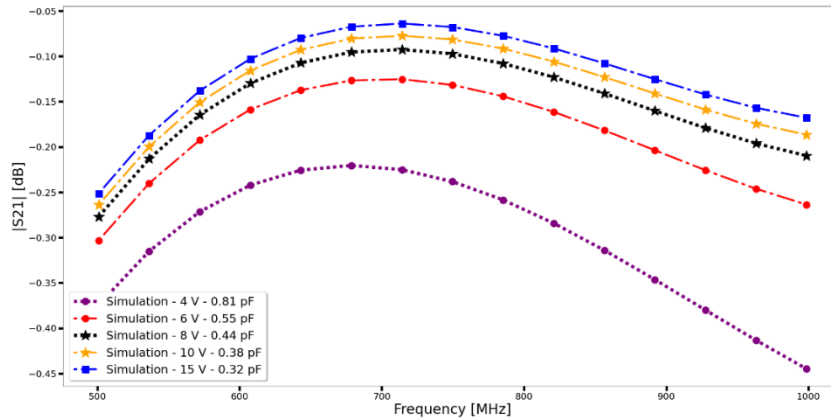


Figure 3.7: Insertion losses of the Coupler Design I with different varactor voltage feeding

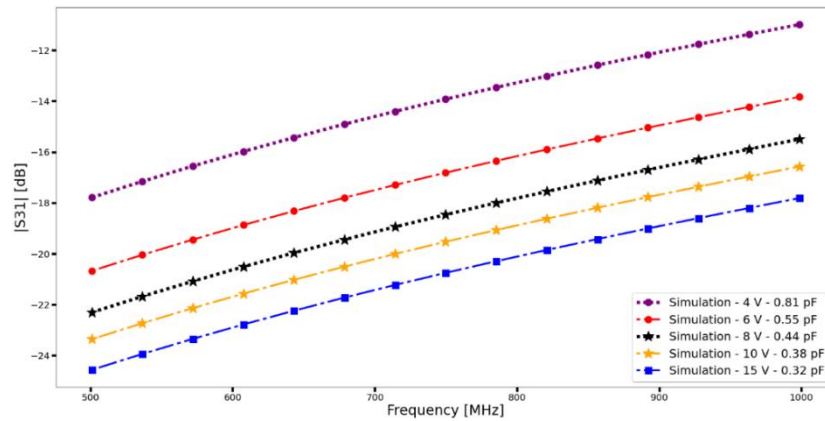


Figure 3.8: Coupling coefficient value of the Coupler Design I with different varactor voltage feeding

Figure 3.9 represents isolation losses of the Coupler Design I with different voltage values span the 500 MHz to 1 GHz frequency range. The isolation is below 50 dB at the entire frequency range.

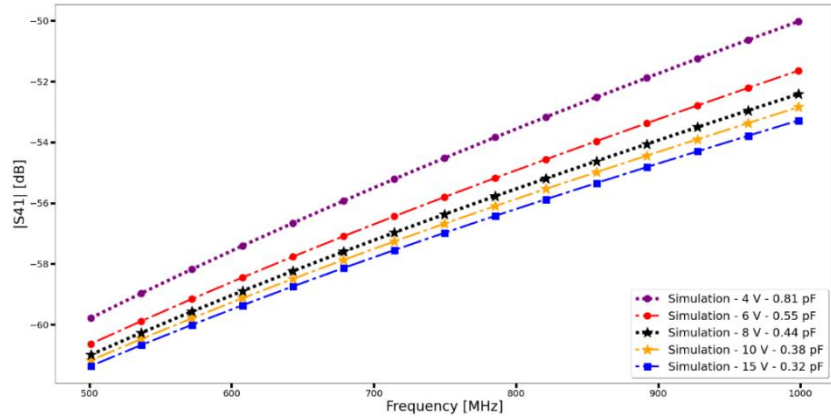


Figure 3.9: S41 numerical calculation results the Coupler Design I with different varactor voltage feeding

3.2 Design and Numerical Calculation Results of the Coupler Design II

Coupler Design II has been planned to be created within the scope of the project consists of six layers as shown in Figure 3.10. These six layers consist of the metallic ground plane, dielectric material, resonator structure, space, dielectric material, and directional coupler structure from bottom to top respectively. It has been planned to establish the electronic controllability required in the multi-layer electronic controlled vertical integration coupler design in the resonator structure. Defected ground structure (DGS) has been utilized to ensure 2.45 GHz operating frequency.

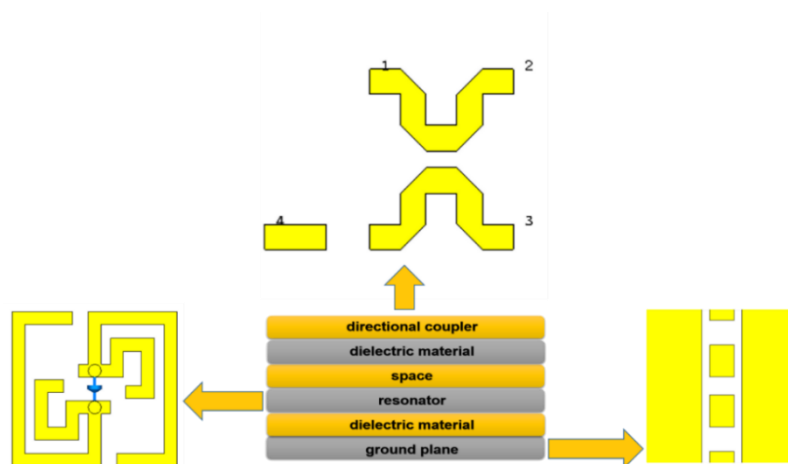


Figure 3.10: Layout of the Coupler Design II

Figures 3.11, 3.12, and 3.13 show the proposed electronically tunable vertical directional coupler layers. Table 3.2 lists the circuit characteristics and key physical dimensions of the vertical integration directional coupler. Electronically tunable vertical integration directional coupler has been modeled on Rogers Duroid 4003 of thickness 1.52 mm, a dielectric constant of 3.55, and a loss tangent of 0.001. The overall physical dimension of the proposed 2.45 GHz directional coupler is 20 mm x 20 mm x 3.62 ($0.164\lambda \times 0.164\lambda \times 0.0296\lambda$). λ is the guided wavelength at the 2.45 GHz operating frequency.

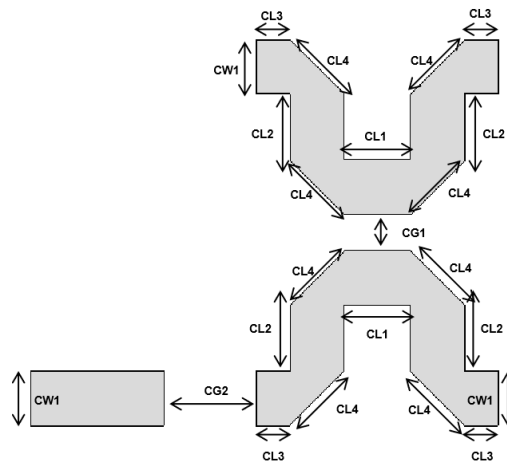


Figure 3.11: Top layer of the Coupler Design II

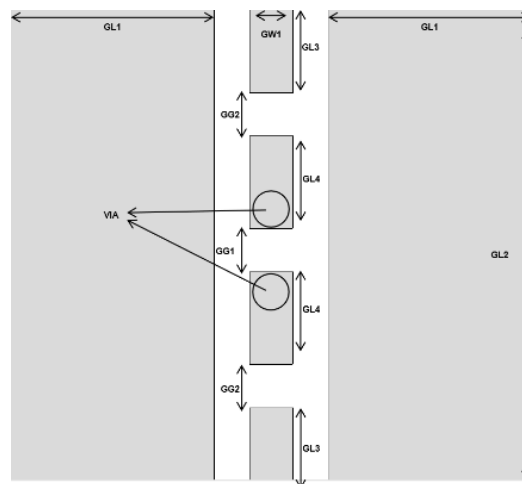


Figure 3.12: Ground plane layer of the Coupler Design II

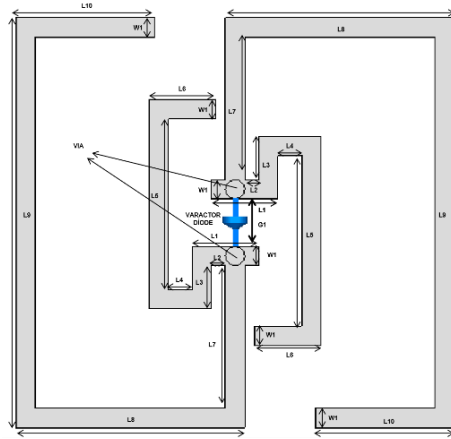


Figure 3.13: Resonator layer of the Coupler Design II

Varactor diode is used to ensure the electronic tunability of the coupling parameters of the proposed electronically controllable directional coupler. The capacitance values of the varactor diode have been remotely set through mobile application. Varactor diode is incorporated within the resonator structure in order to ensure electronic tunability, in addition, to protect DC supply to be fed back to Network Vector Analyzer.

Table 3.2: Geometrical Parameters of Electronically Controllable Directional Coupler Structure and Optimized Dimensions from Numerical Calculations Performed at 2.45 GHz

SYMBOL	VALUE(mm)	SYMBOL	VALUE(mm)
L1	2.82	GL4	9
L2	0.59	GL5	2.57
L3	1.64	GG1	1.5
L4	1.15	GG2	2
L5	2.18	GG3	1.64
L6	1.82	CL1	5
L7	2.5	CL2	2
L8	5.64	CL3	2
L9	9.78	CL4	3
L10	3.82	CL5	1
G1	1.5	CL6	1
W1	0.82	CW1	1
GL1	7.36	CG1	1.5
GL2	2	CG2	1
GL3	5.50		

Figure 3.14 shows that S-Parameter value of the directional coupler without a resonator.

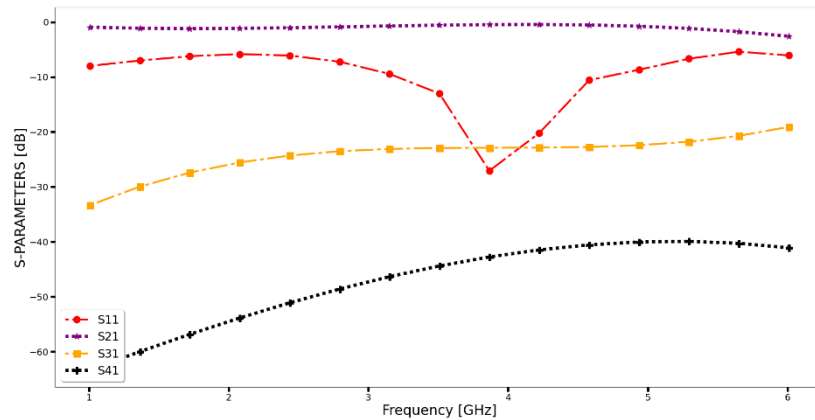


Figure 3.14: S-Parameter value of the directional coupler without resonator

S-Parameter values of the Coupler Design II without varactor diode are shown in Figure 3.15. As can be seen in Figure 3.15, the resonator structure ensured the frequency value of the coupler to reach the 2.45 GHz band. Also coupling value of the Coupler Design II increases.

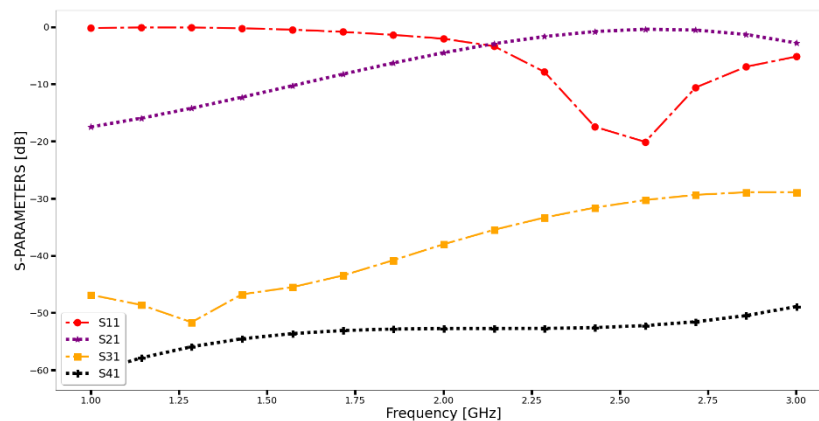


Figure 3.15: S-Parameter value of the vertical integration directional coupler without varactor diode

Figure 3.16 shows that the reflection coefficient values of the Coupler Design II with changing GL4 value at the ground layer. From Figure 3.16, it was observed that the frequency value increase as the GL4 values increased. When the S parameter results

with different GL4 values were analyzed, 9 mm was chosen as the ideal value for 2.45 GHz applications.

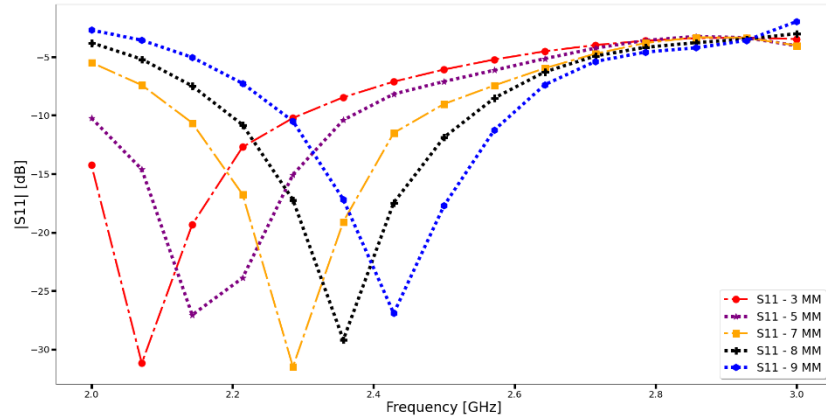


Figure 3.16: Reflection coefficient values of the Coupler Design II

Ideal return losses, insertion losses, and isolation losses are all realized, as shown in Figure 3.17 at the operating frequency of 2.45 GHz under different voltage states (0 – 20). The simulated results of the designed directional coupler show a tuning coupling coefficient range from 13.33 and 22.14 dB at the operating frequency 2.45 GHz as shown in Figure 3.17. The reflection coefficient is ($|S_{11}|$) higher than 10 dB and isolation losses are ($|S_{41}|$) better than 32 dB between biasing voltage value 2 and 20 V (1.2 – 0.30 pF).

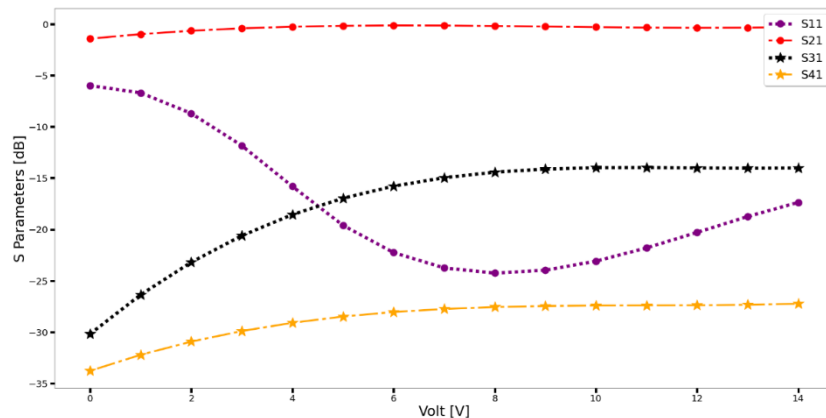


Figure 3.17: S-Parameters results of the Coupler Design II by biasing reverse voltage at 2.45 GHz

Figures 3.18, 3.19, 3.20, 3.21 show the simulated reflection coefficients, insertion loss, coupling, and isolation loss values range from 2 GHz to 3 GHz with reverse biasing voltages of 2 V (1.20 pF), 4 V (0.81 pF), 7 V (0.48 pF), and 20 V (0.30 pF). Figure 3.18 demonstrates return loss of the Coupler Design II with different voltage values across the 2 GHz to 3 GHz frequency range. The reflection coefficient keeps higher than 10 dB at the operating frequency.

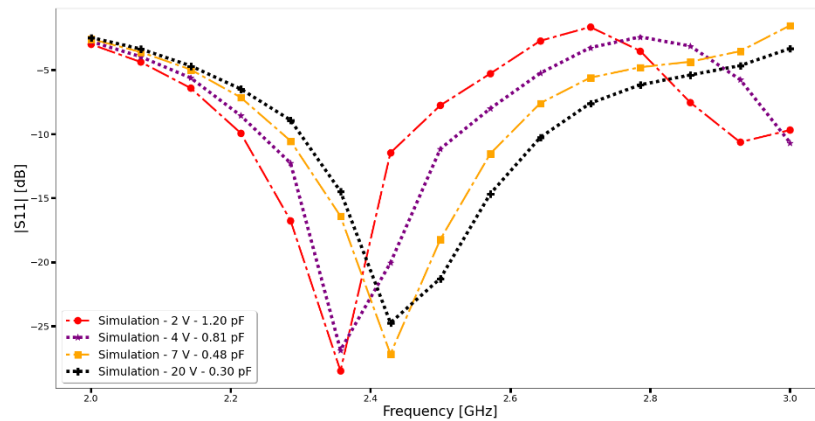


Figure 3.18: Reflection coefficient values of the Coupler Design II with different varactor voltage feeding

Figure 3.19 indicates insertion loss of the Coupler Design II with different reverse biasing volt values across the 2 GHz to 3 GHz frequency range. The insertion losses ($|S21|$) keep lower than 0.85 dB at the operating frequency range.

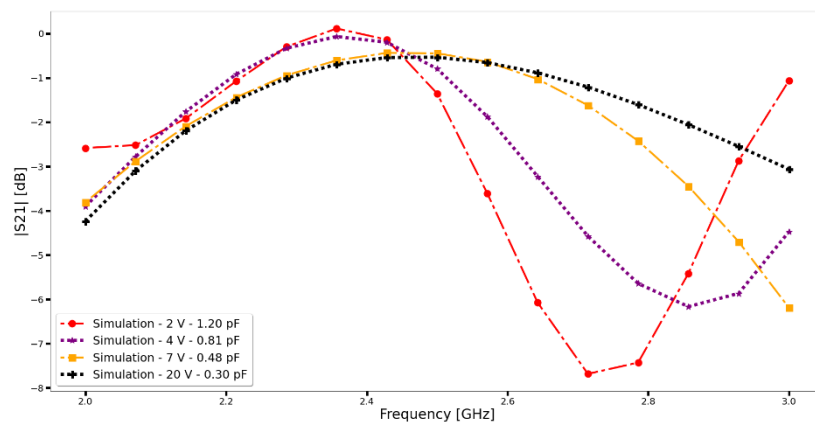


Figure 3.19: Insertion loss values of the Coupler Design II with different varactor voltage feeding

Figure 3.20 shows the simulated coupling value of the Coupler Design II with versus reverse biasing voltage at the frequency range from 2 GHz to 3 GHz.

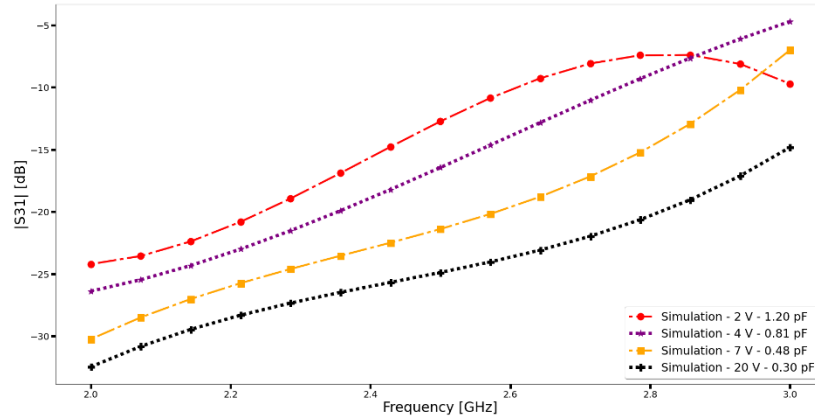


Figure 3.20: The Coupling values of the Coupler Design II with different varactor voltage feeding

Figure 3.21 shows isolation losses of 2.45 GHz directional coupler under the biasing condition (2 V, 4 V, 7 V, and 20 V) over the frequency range from 2 GHz to 3 GHz. The isolation is higher than 32 dB at the all-over frequency range.

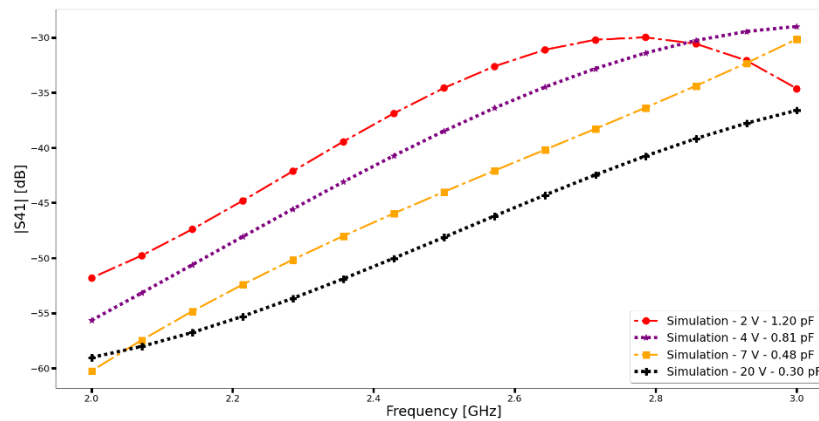


Figure 3.21: The Isolation loss values of the Coupler Design II with different varactor voltage feeding

Chapter 4

Fabrication and Measurement Results of the Electronically Controllable Directional Couplers

In this chapter, the fabrication and measurement results of the proposed couplers are represented.

4.1 Fabrication and Measurement Results of the Coupler Design I

Fabricated Coupler Design I coupler is shown in Figure 4.1.



Figure 4.1: Fabricated Coupler Design I

Electronically controllable directional couplers have been designed and fabricated for experimental demonstration. The results of the S parameter of the electronically controlled directional coupler have been measured via the HP Signal Generator, Signal

Analysis, and Signal Hound Spectrum Analyzer measurement devices in University. The experimental setup required for the S_{11} measurement is shown in Figure 4.2. When measuring the return loss value, the remaining port terminated Dummy Load (50Ω).

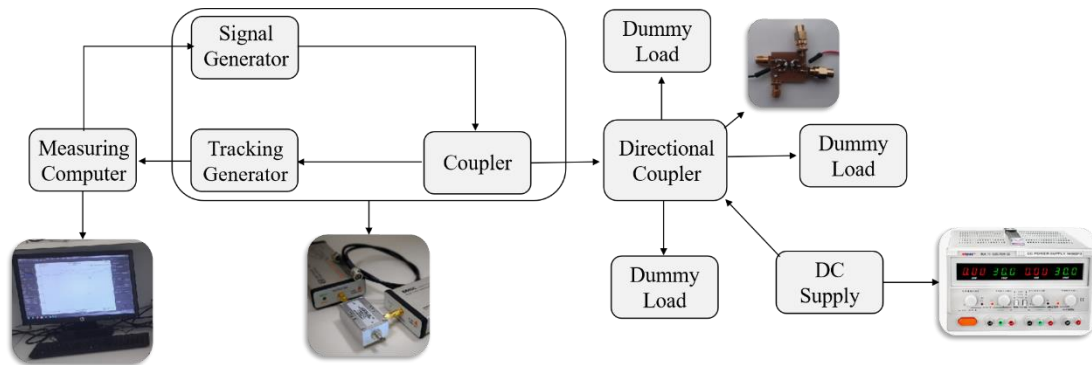


Figure 4.2: Block diagram of the experimental setup for reflection coefficient result

The comparison between the measured and simulated return loss is shown in Figure 4.3 at range 500 MHz to 1000 MHz, when 4 V (0.81 pF), 6 V (0.55 pF), and 15 V (0.32 pF) control voltage levels are applied.

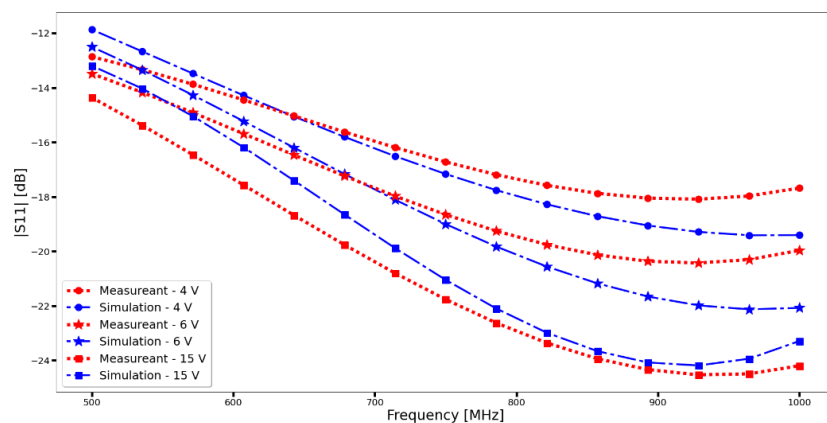


Figure 4.3: The comparison of simulated and measured reflection coefficient value of the Coupler Design I

The experimental setup required for the insertion loss, coupling value, and isolation loss measurement is shown in Figure 4.4. When measuring the coupling, and isolation loss values, the remaining port terminated Dummy Load (50Ω).

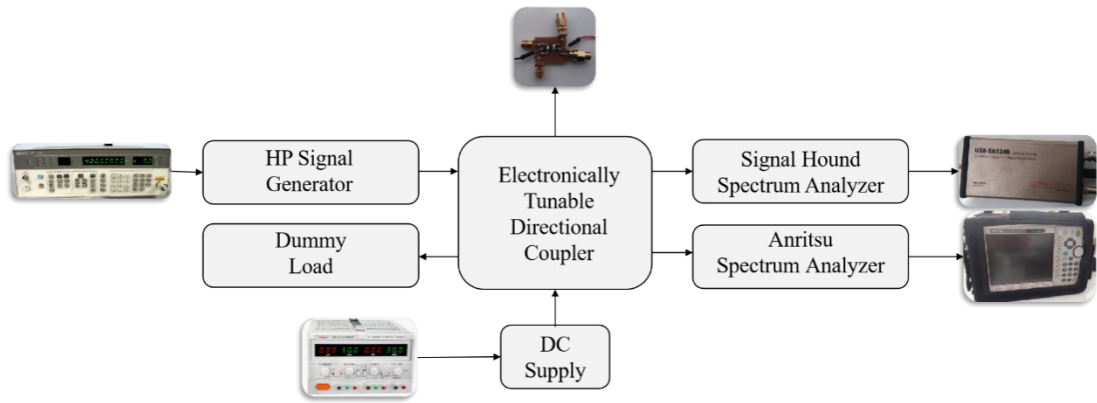


Figure 4.4: Block diagram of the experimental setup for the S21, S31, and S41 S-Parameter results

Figure 4.5 demonstrates the experimental setup. In the experimental setup, the HP signal generator provides the 1mW power to the input port.

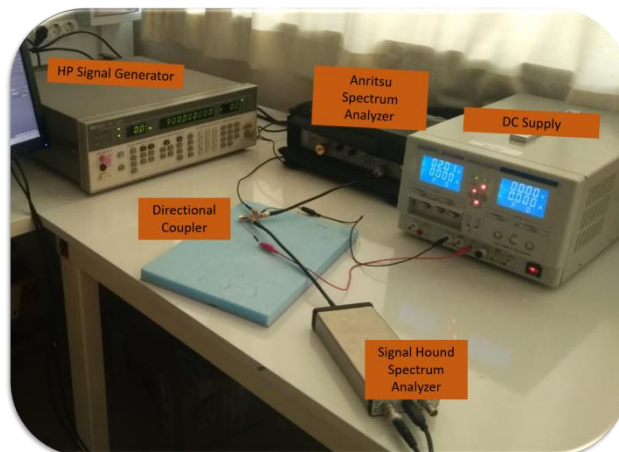


Figure 4.5: The experimental setup for the S21, S31, and S41 S-Parameter results

The power level in the transmission port is measured using an Anritsu spectrum analyzer (S21). The power level in the coupling port is measured by the Signal Hound spectrum analyzer (S31). The power level in the isolation port is measured by the Signal Hound spectrum analyzer (S41). The remaining port ended 50 when the coupling factor and isolation were measured.

Figures 4.3, 4.6, 4.7 and 4.8 show the comparison of measured and simulated insertion loss, coupling value, and isolation at range 500 MHz to 1000 MHz, when 4 V (0.81

pF), 6 V (0.55 pF), and 15 V (0.32 pF) control voltage levels are applied. It's clear that the simulated and measured findings are similar.

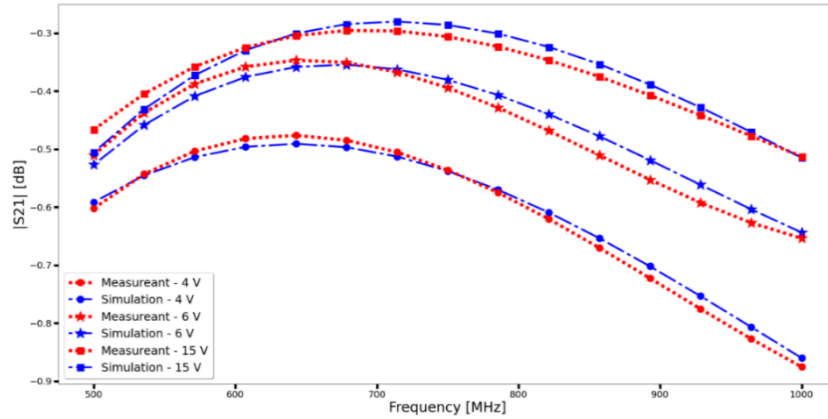


Figure 4.6: The comparison of simulated and measured reflection coefficient value of the Coupler Design II

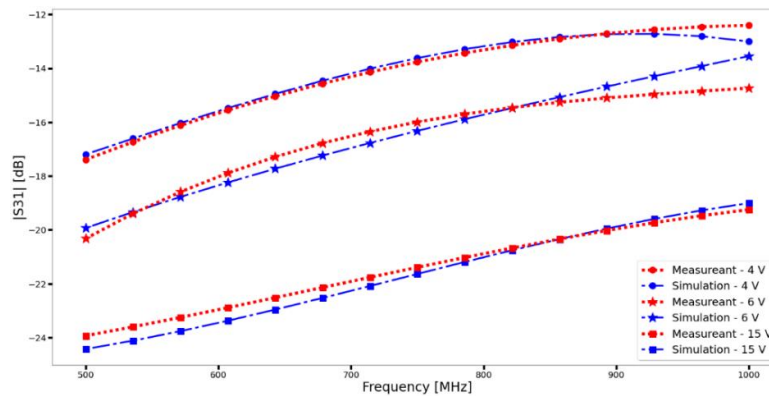


Figure 4.7: The comparison of simulated and measured coupling value of the Coupler Design I

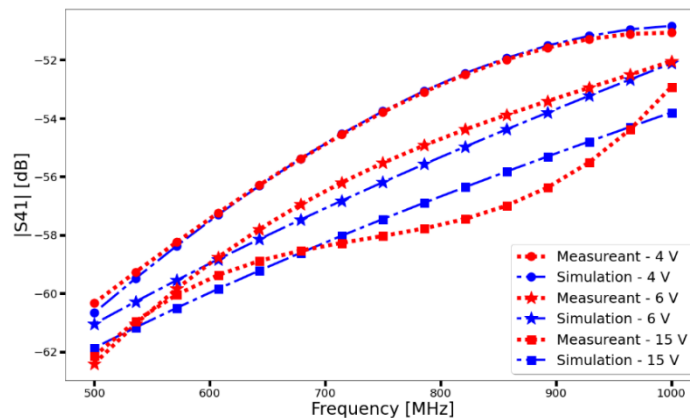


Figure 4.8: The comparison of simulated and measured reflection isolation loss of the Coupler Design I

4.2 Fabrication and Measurement Results of the Coupler Design II

Fabricated Coupler Design II coupler is shown in Figure 4.9.



Figure 4.9: Fabricated Coupler Design II

Varactor diode is used to ensure the electronic tunability of the coupling, directivity, and isolation parameters of the proposed smart directional coupler. The capacitance values of the varactor diode have been remotely set through the Bluetooth-controlled biasing network. In this coupler design, unlike the first 900 MHz electronically tunable directional coupler design, varactor diode has been incorporated within the resonator structure in order to protect DC supply to be fed back to Network Vector Analyzer. In this way, there is no need to use SMD capacitor components in the coupler structure, which are used to prevent damage to the measuring devices and cause RF power loss. DC supply has been provided ground plane layer by via.

Anritsu & Signal Hound Spectrum Analyzer have been used to make the S-Parameters measurements across the 2 GHz to 3 GHz frequency range. The setup for measurement of S_{11} of 2.45 GHz electronically tunable vertical integration directional coupler is shown Figure 4.10.

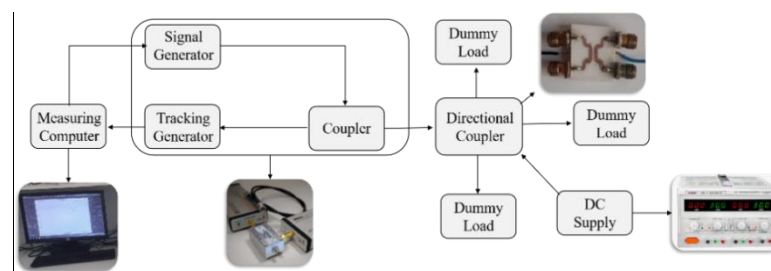


Figure 4.10: Block diagram of the experimental setup of the Coupler Design II for S_{11} S-Parameter results

Figure 4.11 demonstrates the experimental setup.

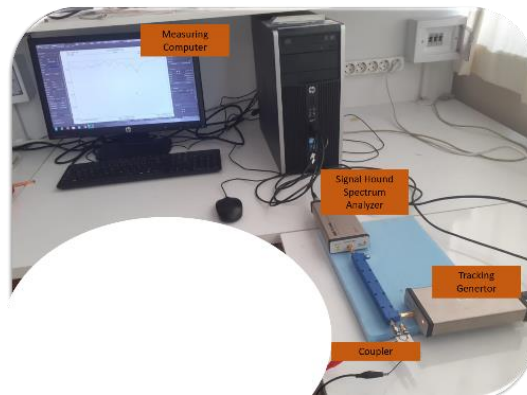


Figure 4.11: The experimental setup for the S11 S-Parameter results

The experimental setup required for the insertion loss, coupling value, and isolation loss measurement is shown in Figure 4.12. When measuring the coupling, and isolation loss values, the remaining port terminated 50 Ω .

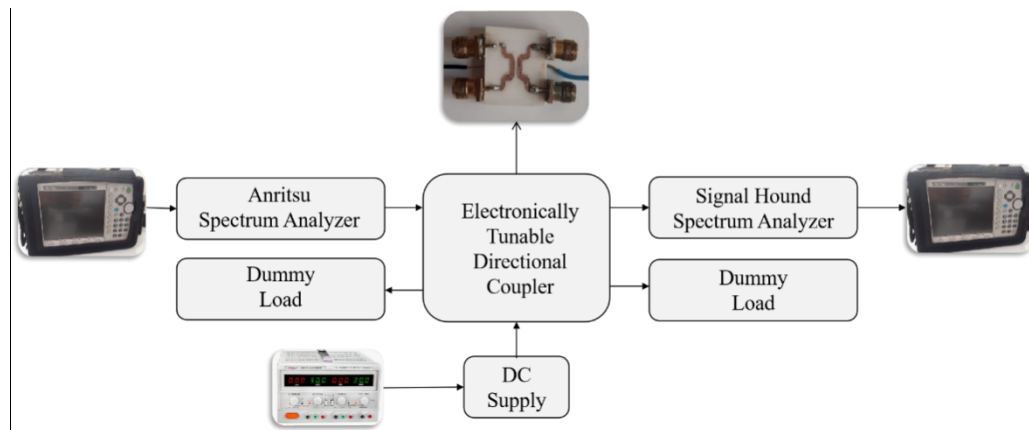


Figure 4.12: Block Diagram of the Experimental Setup of the Vertical Integration Directional Coupler S31 S-Parameter results

Figure 4.13 demonstrates the experimental setup. In the experimental setup, the HP signal generator provides the 1mW power to the input port.

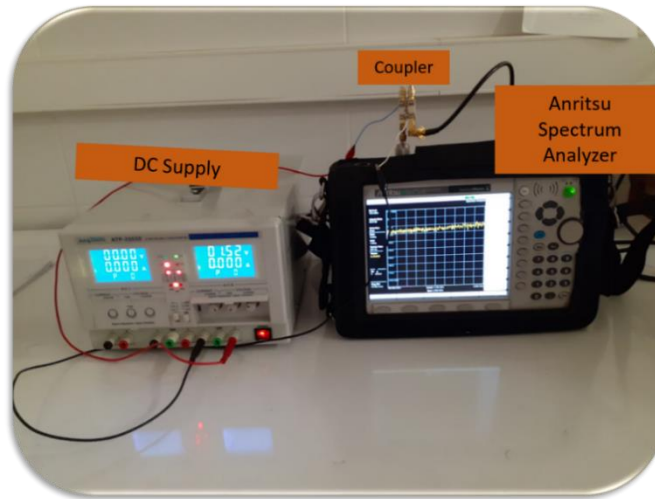


Figure 4.13: The experimental setup for the S21, S31, and S41 S-Parameter results

The power level in the transmission port is measured using an Anritsu spectrum analyzer (S21). The power level in the coupling port is measured by the Signal Hound spectrum analyzer (S31). The power level in the isolation port is measured by the Signal Hound spectrum analyzer (S41). The remaining port ended 50 when the coupling factor and isolation were measured.

Figures 4.14, 4.15, 4.16, 4.17 show the comparison of measured and simulated insertion loss, coupling value, and isolation at range 2 GHz to 3 GHz, when 2 V (1.2 pF), 7 V (0.48 pF), and 16 V (0.32 pF) control voltage levels are applied. It's clear that the simulated and measured findings are similar.

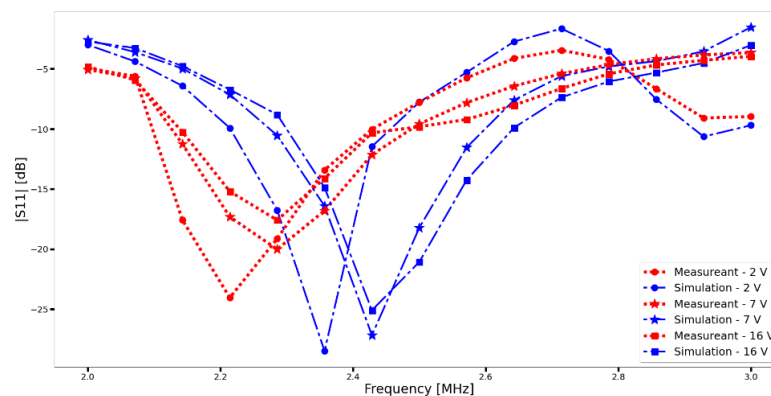


Figure 4.14: The comparison of simulated and measured reflection coefficient value of the Coupler Design II

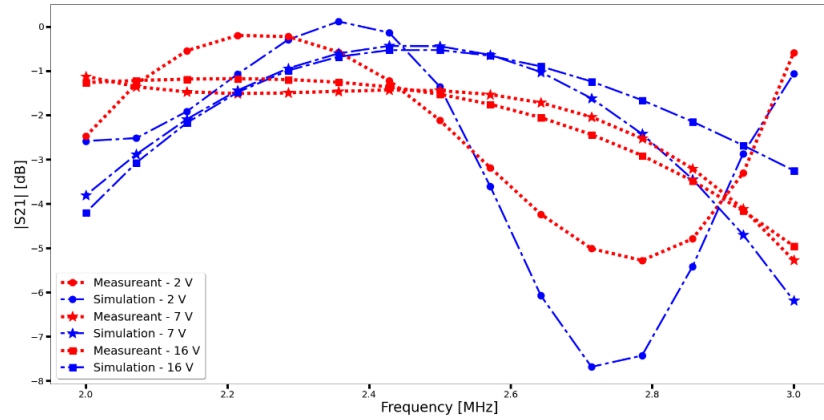


Figure 4.15: The comparison of simulated and measured insertion loss value of the Coupler Design II

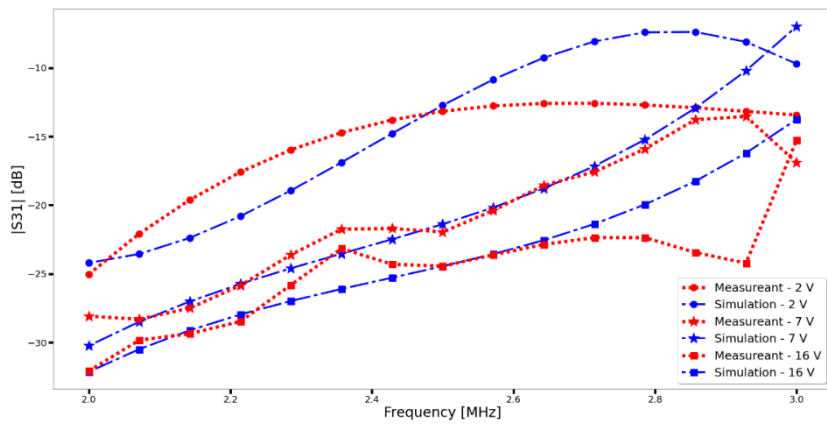


Figure 4.16: The comparison of simulated and measured coupling value of the Coupler Design II

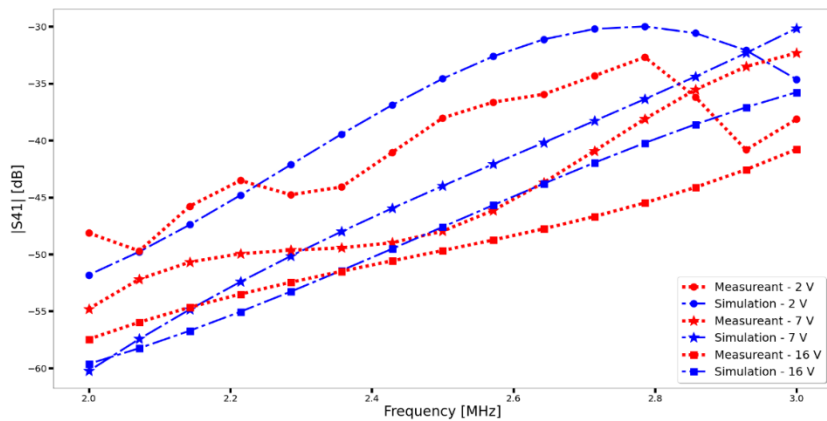


Figure 4.17: The comparison of simulated and measured isolation loss of the Coupler Design II

Chapter 5

Machine Learning Algorithm for Smart and Remotely Controllable Directional Couplers

In this chapter, a brief literature review on the use of machine learning in microwave systems has been presented. Data collection, analysis of data, and selection of the appropriate machine learning algorithm have been out to be used in machine learning.

Computational statistics are used to find a mathematical model that describes input and output data in this field of Artificial Intelligence (AI). A data-driven archetype is a built mathematical model that may be used in place of an analytical equivalent. The data-driven model can handle regression difficulties because it can interpolate output depending on unknown input [41]. Regression is one of the most fundamental methods for prediction in the field of machine learning. Regression involves fitting a function to the given data and attempting to forecast the outcome for the future. This function-fitting serves two functions. This purpose is interpolation and extrapolation.

In many microwave applications nowadays, ML is one of the fast-growing fields that has a wide range of applications. ML is a subclass of artificial intelligence that employs computational statistics to discover a mathematical model that describes input and output data. Over the last few years, Machine learning algorithms have been utilized for different purposes in various fields. Some of these fields are beam control for phased array antenna system [40–42] position detection of the RFID tags [45], optimization [45, 46], failure diagnosis of phased array antenna system [40, 47] antenna selection problem [49] and adaptive spherical near field antenna measurement [50].

The purpose of using machine learning in this thesis is to decide the output voltage value through the prediction-based machine learning algorithm where the training data have been obtained experimentally in the determined frequencies.

In this thesis ML model consist of three components as shown in Figure 5.1.

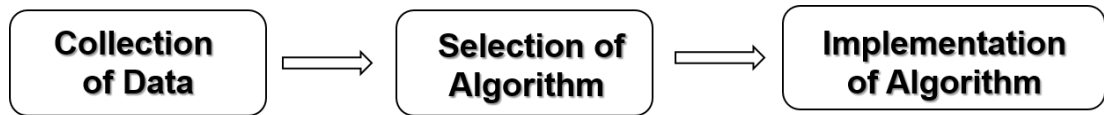


Figure 5.1: ML model of the smart coupler systems

For the parameter prediction to be used in both designs, 192 separate data have been collected by the measurement setup in Anritsu Spectrum Analyzer. Mathematical criteria such as Root Mean Square Error (RMSE), Mean Square Error (MSE), and R-Squared (R^2) value have been used for prediction verification. See Appendix B for RMSE, MSE, and R^2 metric explanations.

5.1 Collection of Data for Smart Coupler Designs

Within the scope of this section, the data required for training, verification, and testing of the machine learning have been collected through experimentally from the measurement systems in Figure 5.2, 5.3 through the Anritsu spectrum analyzer.

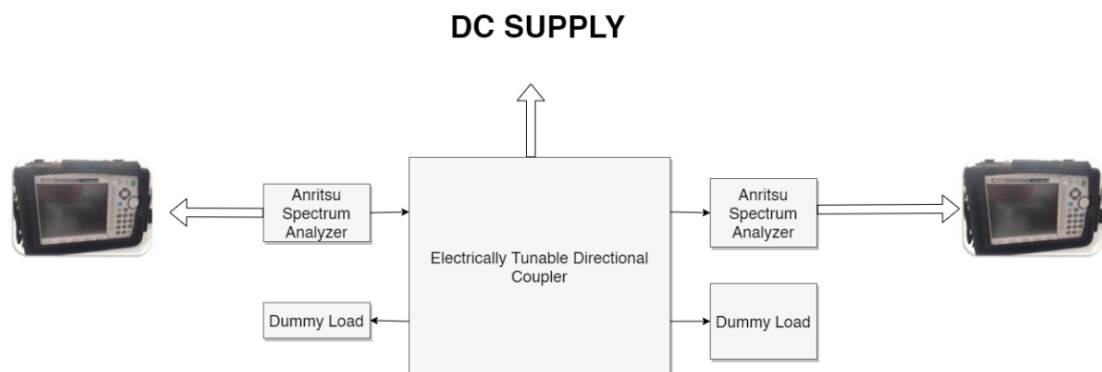


Figure 5.2: Block diagram of the measurement system for S21

For the parameter prediction for Coupler Design I, 192 data have been collected by the measurement setup in Anritsu & Signal Hound Spectrum Analyzer at frequency range 500 to 1000 MHz with the volt ranges between 0.5 and 15.5 volts with 1 Volt difference. 96 data have been collected for S21 and 96 data have been collected for S31.

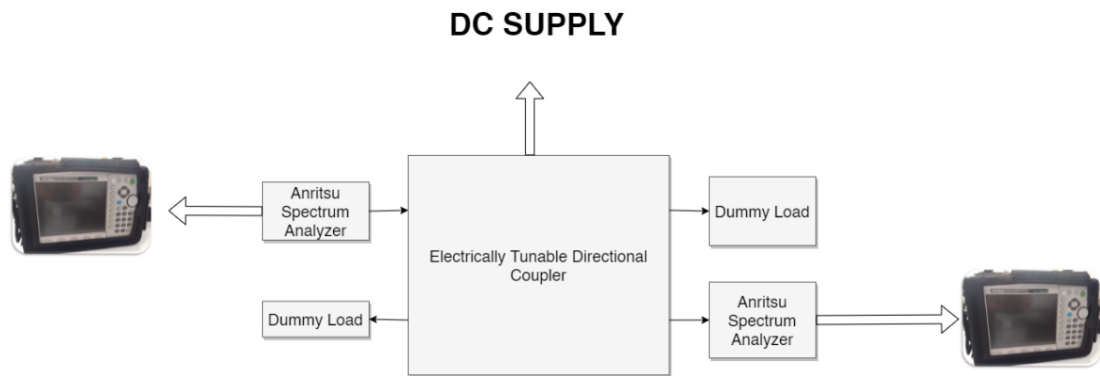


Figure 5. 3: Block diagram of the measurement system for S31

900 MHz applications dataset distribution to give machine learning algorithm as input are shown in Table 5.1. The measurement data was separated into two sections, with a ratio of 66 percent for training and 34 percent for testing procedures of machine learning algorithms, respectively.

Table 5.1: 900 MHz applications dataset

Items	Feeding Voltage (V)	Frequency (MHz)
Inteval	0.5-15.5	500 – 1000
Step	1	100
Number	16	6

For the parameter prediction for Coupler Design II, 192 data have been collected by the measurement setup in Anritsu & Signal Hound Spectrum Analyzer at frequency range 2 to 3 GHz with the volt ranges between 0.5 and 15.5 volts with 1 Volt difference. 96 data have been collected for S21 and 96 data have been collected for S31.

2.45 GHz dataset distribution to give machine learning algorithm as input are shown in Table 5.2. The measurement data was separated into two sections, with a ratio of 66 percent for training and 34 percent for testing procedures of machine learning algorithms, respectively.

Table 5.2: 2.45 GHz applications dataset.

Items	Feeding Voltage (V)	Frequency (MHz)
Interval	0.5-15.5	2000 - 3000
Step	1	200
Number	16	6

5.2 Selection of Machine Learning Algorithm for Coupler Design I

Different regression algorithms have been applied to the prediction of S21 and S31 parameters and to select an ideal regression algorithm with a high prediction rate by using the measurement data taken during the thesis measurement period. There are 192 measurement data in the data set. Voltage and frequency values have been given as input to the ML models. S21 and S31 have been the outputs of the ML models. R2 value, MSE, RMSE have been determined for prediction metrics of the ML algorithms.

Table 5.3 represents regression algorithm performance comparison for S21 output value with different algorithms.

Table 5.3: Regression algorithm performance comparison for S21 output value

Regression Algorithm	Metric	Results
Linear	R2	0.52
	MSE	0.0422
	RMSE	0.205

Table 5.3 (continued)		
	R2	0.99
Polynomial 3 rd Degree	MSE	0.000652
	RMSE	0.0255
	R2	0.95
Decision Tree (max_depth=2)	MSE	0.0042
	RMSE	0.065
	R2	0.99
Gradient Boosting	MSE	4.074
	RMSE	0.0020
	R2	0.52
Bayesian Ridge	MSE	0.042
	RMSE	0.21

Table 5.4 shows regression algorithm performance comparison for S31 output value with different algorithms.

Table 5.4: Regression algorithm performance comparison for S31 output value

Regression Algorithm	Metric	Results
	R2	0.52
Linear	MSE	0.0422
	RMSE	0.205
	R2	0.99
Polynomial 3 rd Degree	MSE	0.027
	RMSE	0.165
	R2	0.83
Decision Tree (max_depth=2)	MSE	3.31
	RMSE	1.82
	R2	0.99
Gradient Boosting	MSE	0.00098
	RMSE	0.031
	R2	0.87
Bayesian Ridge	MSE	2.4
	RMSE	1.54

As shown in Table 5.3 and Table 5.4 3rd order polynomial regression with the best prediction metric has been chosen for the parameter prediction of S21 and S31 values. The R2 value is larger than 0.99, the MSE value is less than 0.027 and RMSE is less than 0.165. The polynomial regression equation is stated has been obtained in Equation 5.1.

$$f(x) = p1.x^3 + p2.x^2 + p3. x + p4 \quad (5.1)$$

5.3 Implementation of Machine Learning Algorithm for Coupler Design I

Voltage and frequency values have been given as input to the ML models. S21 and S31 have been the outputs of the ML models. In Raspberry Pi 3b+, the output voltage values have been decided through the prediction-based machine learning algorithms where the training data have been obtained from the measurement results. It is important to ensure the correct S21 and S31 values of the smart directional coupler have been obtained for the performance parameter settings on the smartphone via the Android user interface. Table 5.5 shows the polynomial constants of the regression equation at three different frequencies for S21 and S31.

Table 5.5: Constant of third degree polynomial regression equation for Coupler Design I

Symbol	p1	p2	p3	p4
S21_880	0.000979	-0.03275	0.3678	-2.307
S21_900	0.001083	-0.03443	0.3537	-2.397
S21_920	0.001188	-0.03869	0.4087	-1.965
S31_880	0.003135	-0.02106	-1.338	-7.286
S31_900	0.008041	-0.1197	-0.8851	-7.317
S31_920	0.003236	-0.02706	-1.181	-6.504

In Figure 5.4 the prediction curves resulting from the polynomial regression model at 880,900, and 920 MHz frequencies are shown.

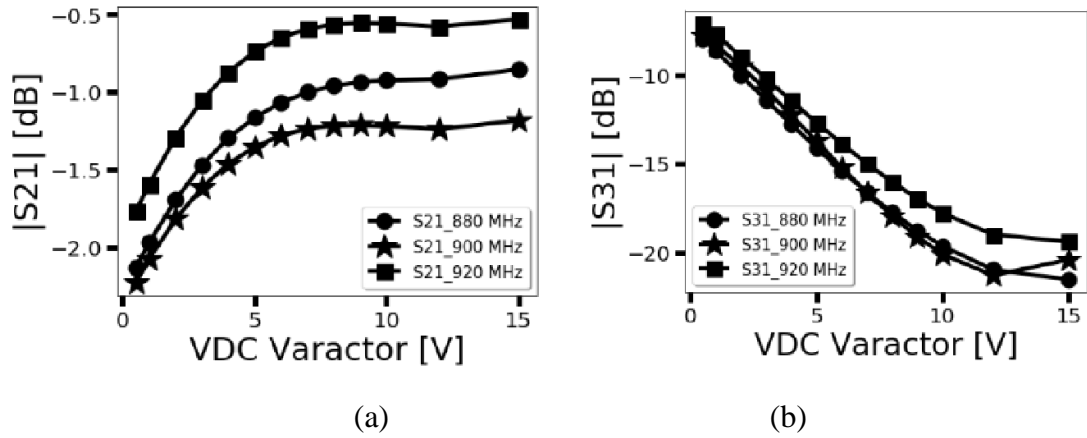


Figure 5. 4: The sample of the prediction curve for 880,900, and 920 MHz: a) $|S_{21}|$ and b) $|S_{31}|$

5.4 Selection of Machine Learning Algorithm for Coupler Design II

Versatile different regression algorithms have been applied to the prediction of volt parameters and to select ideal regression algorithm with a high prediction rate by using the measurement data taken during the thesis measurement period. There are 192 measurement data in the data set. S_{31} and frequency values have been given as input to the ML models. Volt has been the output of the ML models. The R^2 value, the MSE, RMSE have been determined for prediction metrics of the ML algorithms.

Table 5.6 shows regression algorithm performance comparison for S_{31} output value with different algorithms. As shown in Table 5.6 3rd order polynomial regression with the best prediction metric has been chosen for the parameter prediction of S_{31} values. The R^2 value is larger than 0.99, the MSE value is less than 0.27 and RMSE is less than 0.52. The polynomial regression equation is stated has been obtained in Equation 5.2.

$$f(x) = p1.x^3 + p2.x^2 + p3. x + p4 \quad (5.2)$$

Table 5.6: Regression algorithm performance comparison for output value

Regression Algorithm	Metric	Results
Linear	R2	0.6
	MSE	13
	RMSE	3.61
Polynomial 3 rd Degree	R2	0.99
	MSE	0.27
	RMSE	0.52
Decision Tree (max_depth=5)	R2	0.78
	MSE	7.03
	RMSE	2.65
Gradient Boosting	R2	0.94
	MSE	2.13
	RMSE	1.45
Random Forest	R2	0.60
	MSE	13.05
	RMSE	3.61

5.5 Implementation of Machine Learning Algorithm for Coupler Design II

Frequency and S31 values have been given as input to the ML models. Voltage value has been the output of the ML models. In Raspberry Pi Pico, the output voltage values have been decided through the prediction-based machine learning algorithms where the training data have been obtained from the measurement results. It is important to ensure the correct voltage value of the smart directional coupler has been obtained for the performance parameter settings on the smartphone via the Android user interface.

Table 5.7 shows the polynomial constants of the regression equation at three different frequencies for S31.

Table 5.7: Constant of third degree polynomial regression equation for Coupler Design II

Symbol	p1	p2	p3	p4
S31_2400	0.009178	-0.4557	7.974	-46.28
S31_2450	0.008229	-0.3861	6.453	-35.41
S31_2500	0.0071	-0.3127	4.988	-25.71

In Figure 5.5 the prediction curves resulting from the polynomial regression model at 2400, 2450, and 2500 MHz frequencies are shown.

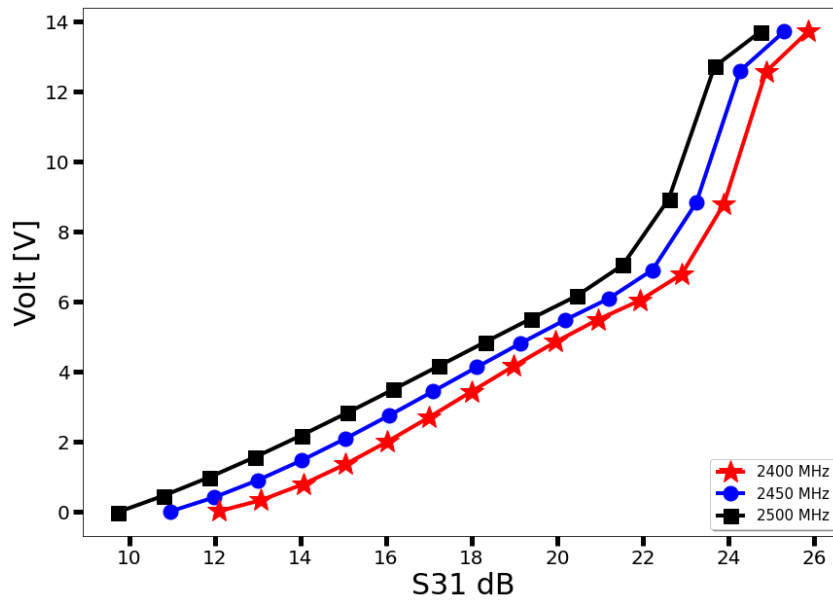


Figure 5. 5: The sample of the prediction curve for 2400 MHz, 2450 MHz, and 2500 MHz

Chapter 6

Integration of the Electronically Controllable Smart Coupler System

In this chapter, microcontroller-based system smart control of electrically tunable directional coupler systems is represented. Electronically controllable smart directional coupler system design consists of four main sections. The first part is the directional coupler design. The second part is Android interface designs. The third part is the DC supply to drive the varactor diode. And last part is system integration. In chapter 3, directional couplers have been designed, and in chapter 4 these couplers have been fabricated.

6.1 Android Interface Designs

Android applications can be created using either IDEs such as Android Studio (AS) or MIT's App Inventor. In this thesis, two different interface design approach has been realized for two different directional couplers. For both user-based interfaces, the Bluetooth connection must be provided to ensure data flow between the android smartphone and microcontroller. To ensure this situation, firstly the devices must be paired.

6.1.1 Android Interface Design for Coupler Design I

This interface design has been prepared by using the Java language in Android Studio integrated development environment for Coupler Design I. The interface outline is as shown in Figure 6.1. This system has been used Raspberry Pi 3 B+ as a microcontroller. That microcontroller has a Bluetooth module as an integrated.

The terminal is the easiest way to link your Bluetooth devices with your Raspberry Pi 3 B+.

- i. Launch a new Terminal window from the Raspberry Pi desktop.
- ii. Enter the administrator password after typing `'sudo bluetoothctl'`.
- iii. Next, type `'agent on'` and click enter. Then, in the search box, type `'default-agent'` and click enter.
- iv. Type `'scan on'` once again and press enter. The special addresses of every single Bluetooth devices around the Raspberry Pi 3 B+ will look something similar an alphanumeric `XX:XX:XX:XX:XX:XX`.
- v. type `'pair [device Bluetooth address]'` to pair the device.

After two devices are paired, connect button must be pressed to connect devices by selecting Raspberry Pi 3 B+.

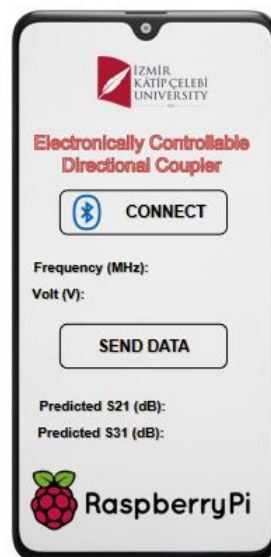


Figure 6.1: Android interface outline design for a system of the Coupler Design I

With the Android interface application to be designed, the voltage level required to drive the varactor diode and the frequency information required to operate the

directional coupler is received as input from the user and transmitted to the microcontroller via Bluetooth protocol. In addition, S21 and S31 values obtained from the microcontroller with the help of the artificial neural networks and high performance is be taken via Bluetooth protocol and displayed to the user. Third Degree Polynomial Regression has been utilized for the parameter prediction of S21 and S31 values by Raspberry Pi 3 B+.

6.1.2 Android Interface Design for Coupler Design II

The interface design has been prepared through a visual programming environment as known MIT APP Inventor for Coupler Design II. The graphical user interface outline is as shown in Figure 6.2. This system has been used Raspberry Pi Pico as a microcontroller without a Bluetooth module. The Bluetooth module (HC-06) is wired to the Raspberry Pi Pico board to guarantee continuous with the Android phone.

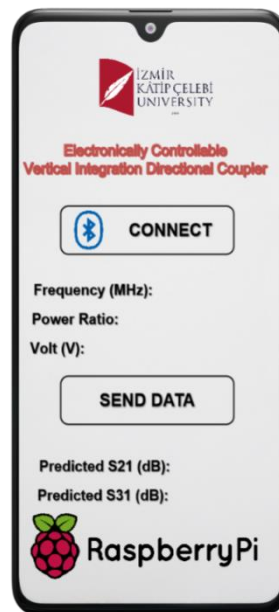


Figure 6.2: Android interface outline design for a system of the Coupler Design II

The module uses the Bluetooth 2.0 protocol and can only be used as a slave device. The communication with this HC-06 module is done through the UART interface. The module is powered by a controlled +5V power source. Android phone pair with

standard password 0000 or 1234. After two devices are paired, connect button must be pressed to connect devices by selecting the HC-06 module.

With the Android interface application to be designed, the frequency information and power division ratio required to operate the directional coupler has been received as input from the user. The voltage level required to drive the varactor diode and S21, S31 values have been obtained from the application with the help of the artificial neural networks have been displayed to the user, also volt value transmitted to the microcontroller via Bluetooth protocol.

6.2 DC Supply

Varactor diode is used to ensure the electronic tunability of the coupling, directivity, and isolation parameters of the proposed smart directional couplers. The capacitance values of the varactor diode have been remotely set through Bluetooth-controlled biasing networks. Varactor diode has an adjustable capacitance range of 2.2 to 0.3 pF and reverses voltages that range from 0 to 20 V.

Pulse Width Modulation is a default output Raspberry Pi 3b+ Microcontroller and Raspberry Pi Pico. It is required a DC supply to drive a varactor diode, so it becomes necessary to convert a PWM to a DC signal. The DAC circuit provides from input 0-3.3 Volt PWM to 0-3.3V analog output. Thanks to LM741 the maximum 3.3 Volt PWM signal that DAC converts to analog signal is increased by 5 times to 16.5 DC Volt. See Appendix C for the amplifier schematic. CST Microwave Studio is used to realized amplifier design. The amplifier has been fabricated with the help of MITS Eleven Lab brand PCB device. Figure 6.3 shows the designed and fabricated amplifier.

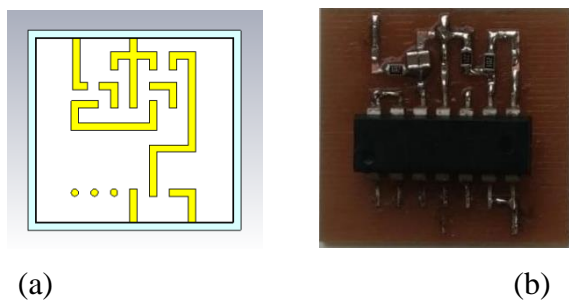


Figure 6.3: Amplifier design (a), Fabricated amplifier (b)

6.3 System Integration and Working Principle

Figure 6.4 represents a block diagram of the remote controller Coupler Design I system connected to Raspberry Pi 3b+ microcontroller to reverse bias the varactor diode through an Android-based RF component-specific 900 MHz applications in a remote system.

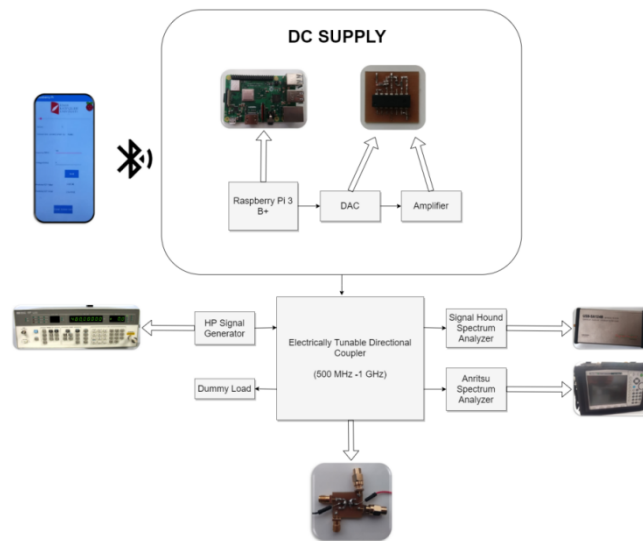


Figure 6.4: Electronically controllable system design for first directional coupler

The system integration and validation setup of the Coupler Design I for the S₂₁, S₃₁ S-Parameter results show in Figure 6.5.

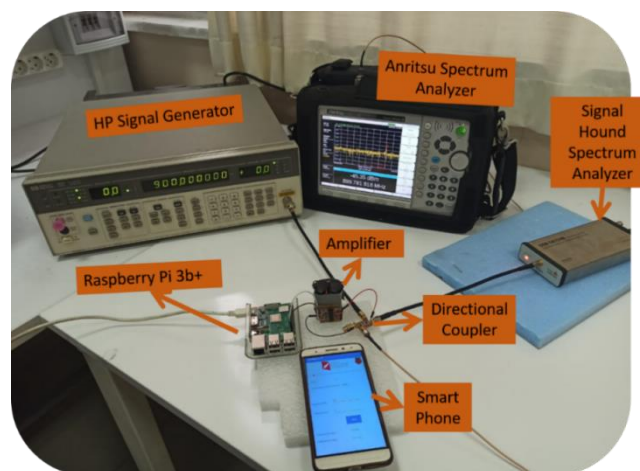


Figure 6.5: The system integration and validation setup for the S₂₁, S₃₁

Figure 6.6 shows a block diagram of the remote controller Coupler Design II system design for vertical integration directional coupler connected to Raspberry Pi Pico microcontroller to drive the varactor diode.

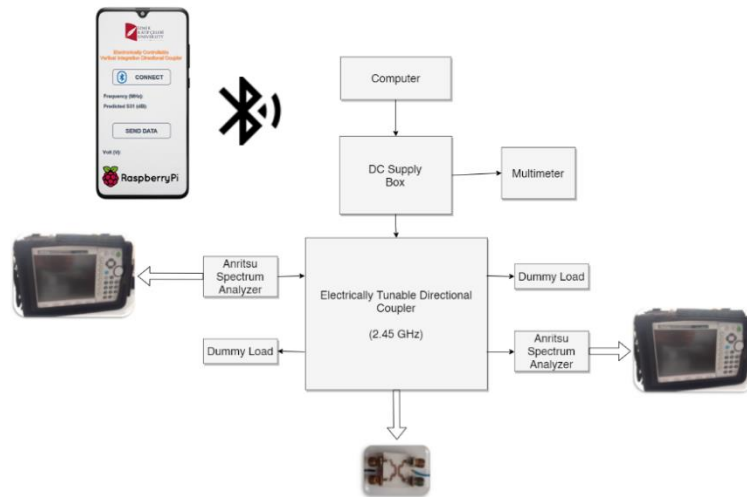


Figure 6.6: Electronically controllable system design for vertical integration directional coupler

The system integration and validation setup of the Coupler Design II for the S21, S31 S-Parameter results show in Figure 6.7.

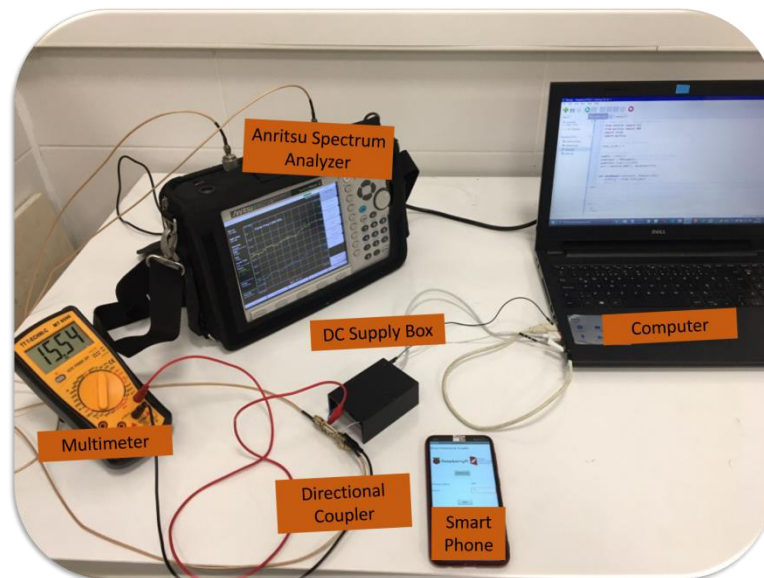


Figure 6.7: The system integration and validation setup of the Coupler Design II for the S31 and Volt

The system flowchart diagram of the Coupler Design I is shown in Figure 6.8 and Figure 6.9. Figure 6.8 demonstrates the application working principle and communication with Raspberry Pi 3 B+. Figure 6.9 shows the flowchart after the application starts.

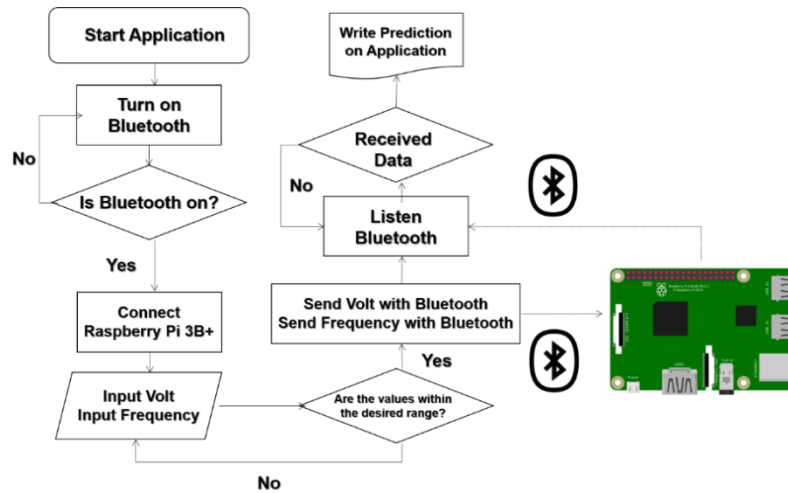


Figure 6.8: Flowchart diagram of the Coupler Design I application side

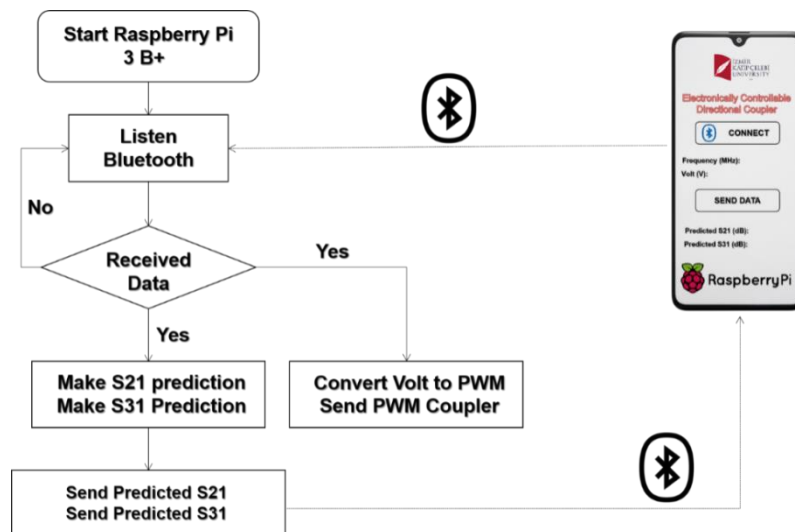


Figure 6.9: Flowchart diagram of the Coupler Design I Raspberry Pi 3 B+ side

The system flowchart diagram of the Coupler Design II is shown in Figure 6.10 and Figure 6.11. Figure 6.10 demonstrates the application working principle and communication with Raspberry Pi Pico via HC-06. Figure 6.11 shows the flowchart after the application starts.

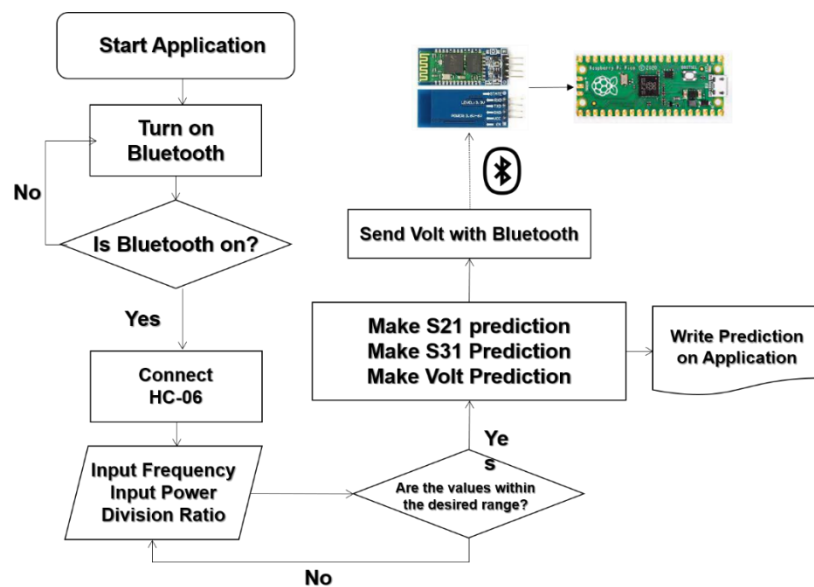


Figure 6.10: Flowchart diagram of the Coupler Design II application side

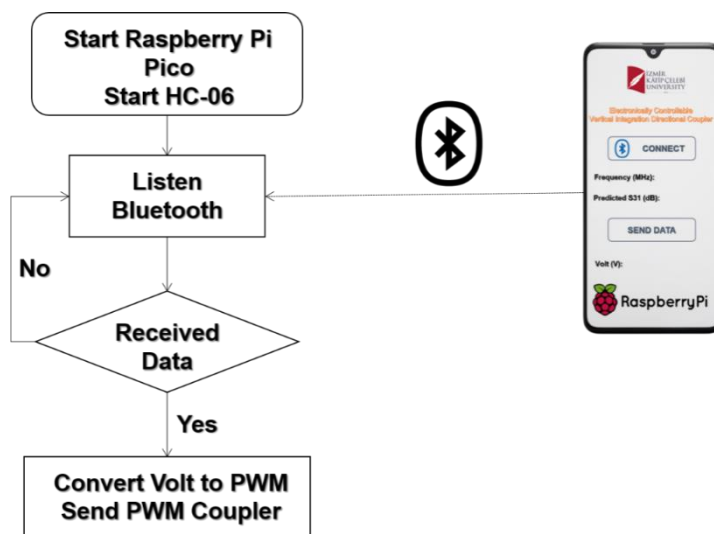


Figure 6.11: Flowchart diagram of the Coupler Design II Raspberry Pi Pico

Chapter 7

Conclusion

The concluding remarks are conducted in this chapter. In this thesis, a single varactor diode-based balanced compact smart system with two different directional couplers has been proposed for IoT applications. A smart system of directional couplers was designed, simulated, and validated experimentally. Numerical analysis software based on the Finite-Difference Time-Domain (FDTD) method has been used for the design and numerical calculation of directional couplers. The electrically tunable feature of the smart directional couplers can be successfully accomplished remotely through Bluetooth connection with the intended performance parameters set on the Android application. DC bias voltage control is supplied by using a microcontroller.

The operating frequency band of the Coupler Design I is extending from 500 MHz up to 1 GHz covering the dedicated wide/local area IoT frequency bands ranging from radio frequency identification (RFID) up to mobile network applications. The Coupler Design I prototype has been fabricated on a low-loss Rogers RO4003C substrate. The compact overall size of the first design is 13.66 mm x 15.99 mm x 1.59 mm, ($0.041 \lambda \times 0.048 \lambda \times 0.0047 \lambda$). The high isolation level of more than 50 dB and low return loss higher than 12 dB have been experimentally measured in the whole operating frequency band.

The center frequency of the Coupler Design II is 2.45 GHz covering the dedicated wide/local area IoT frequency bands ranging from radio frequency identification (RFID) up to mobile network applications. The Coupler Design II prototype has been fabricated on low-loss Rogers RO4003C substrate. The overall physical dimension of the proposed 2.45 GHz directional coupler is 20 mm x 20 mm x 3.62 ($0.164\lambda \times 0.164\lambda \times 0.0296 \lambda$). The high isolation level of more than 32 dB and low return loss higher than 10 dB have been experimentally measured in operating frequency.

In this thesis, small discrepancies between the the numerical and experimental results of the proposed directional couplers were largely caused by the parasitic effect of the lumped elements and the fabrication tolerances. The compact directional couplers have high technical potential to be used for smart IoT applications.

Table 7.1 points out the RF performance parameters of the proposed smart coupler structure in comparison to the alternative coupler designs in the literature. According to the analysis Table 7.1, unlike other studies, the proposed directional couplers are controlled via the user interface. In addition, the tunability of the S31 value is provided by the ML algorithm. Coupler Design I and Coupler Design II electrically controllable smart directional couplers have better isolation levels greater than 32 dB and low insertion loss level smaller than 0.9 dB in more compact cell size with only a single varactor diode.

The proposed different configurations offer several advantages, which can be listed as: i) user-friendly DC bias voltage control ii) ideal port isolation and return loss performance; iii) electronic remote controllability of the coupling level; iv) simple design with only a single varactor diode by a single control voltage; v) cheap and compact design; vi) integrity potential to IoT components and systems.

Table 7.1: Comparison of RF performance parameters between the proposed coupler structure and referenced coupler

Items	[6]	[23]	[8]	[10]	Coupler Design I	Coupler Design II
Technology	PCB	PCB	PCB	PCB	PCB	PCB
Tuning Elements	Varactor (4)	Varactor (4)	Varactor (4)	Varactor (3)	Varactor (1)	Varactor (1)
User Based Voltage Control	No	No	No	No	Yes	Yes
ML Implementation	No	No	No	No	Yes	Yes
Return Loss (dB)	>15	>20	>15	>20	>10	>10
Insertion Loss (dB)	<1.8	1.2	-----	<1.3	<0.9	<0.8
Isolation (dB)	>15	>22	>20	>20	>50	>32
Coupling Factor (dB)	0~3	39~29	3.5~4.1	0.7~11.7	4.51~19.37	13.33~22.14
Operating Frequency (GHz)	1-1.5	2.4	2.48	1.7	0.9	2.45
Size ($\lambda*\lambda$)	0.08*0.08	0.65*0.28	0.19*0.15	0.21*0.09	0.041*0.048	0.164*0.164

References

- [1] G. M. Rebeiz, RF MEMS, 1st ed. Newyork: Wiley-Interscience, 2003.
- [2] U. Shah, M. Sterner, and J. Oberhammer, “High-directivity MEMS-tunable directional couplers for 10-18-GHz broadband applications,” *IEEE Trans. Microw. Theory Tech.*, vol. 61, no. 9, pp. 3236–3246, 2013, doi: 10.1109/TMTT.2013.2273763.
- [3] B. Hur and W. R. Eisenstadt, “Tunable broadband MMIC active directional coupler,” *IEEE Trans. Microw. Theory Tech.*, vol. 61, no. 1, pp. 168–176, 2013, doi: 10.1109/TMTT.2012.2228218.
- [4] M. A. Y. Abdalla, K. Phang, and G. V. Eleftheriades, “A compact highly reconfigurable CMOS MMIC directional coupler,” *IEEE Trans. Microw. Theory Tech.*, vol. 56, no. 2, pp. 305–319, 2008, doi: 10.1109/TMTT.2007.913360.
- [5] V. Solomko, B. Tanc, D. Kehrer, N. Ilkov, W. Bakalski, and W. Simbürger, “Tunable directional coupler for RF front-end applications,” *Electron. Lett.*, vol. 51, no. 24, pp. 2012–2014, 2015, doi: 10.1049/el.2015.2601.
- [6] R. Zhang, M. F. Hagag, L. Yang, R. Gomez-Garcia, and D. Peroulis, “A Flexible Quadrature Coupler with Reconfigurable Frequency and Coupling Ratio in Switchable Coupling Direction,” *IEEE Trans. Microw. Theory Tech.*, vol. 67, no. 8, pp. 3391–3402, 2019, doi: 10.1109/TMTT.2019.2918528.
- [7] P. L. Chi, H. M. Lin, and C. P. Chien, “A Tunable Balanced Coupler with Improved Phase Balance and Extended Bandwidth,” *IEEE Access*, vol. 7, pp. 37927–37935, 2019, doi: 10.1109/ACCESS.2019.2906551.
- [8] X. Tan and F. Lin, “A novel rat-race coupler with widely tunable frequency,” *IEEE Trans. Microw. Theory Tech.*, vol. 67, no. 3, pp. 957–967, 2019, doi:

10.1109/TMTT.2018.2889453.

- [9] F. Lin, “Compact Design of Planar Quadrature Coupler with Improved Phase Responses and Wide Tunable Coupling Ratios,” *IEEE Trans. Microw. Theory Tech.*, vol. 66, no. 3, pp. 1263–1272, 2018, doi: 10.1109/TMTT.2017.2783375.
- [10] T. Zhang and W. Che, “A Compact Reconfigurable Coupler with Tunable Coupling Coefficients and Frequencies,” *IEEE Microw. Wirel. Components Lett.*, vol. 27, no. 2, pp. 129–131, 2017, doi: 10.1109/LMWC.2016.2646904.
- [11] X. Shen, Y. Liu, S. Zhou, and Y. Wu, “Coupled-line directional coupler with tunable power division ratio and operating frequency,” *IET Microwaves, Antennas Propag.*, vol. 11, no. 1, pp. 59–68, 2017, doi: 10.1049/iet-map.2016.0067.
- [12] S. Y. Zheng, “Simultaneous Phase-and Frequency-Tunable Hybrid Coupler,” *IEEE Trans. Ind. Electron.*, vol. 64, no. 10, pp. 8088–8097, 2017, doi: 10.1109/TIE.2017.2698423.
- [13] J. Y. Shen *et al.*, “High-directivity single- and dual-band directional couplers based on substrate integrated coaxial line technology,” *IEEE MTT-S Int. Microw. Symp. Dig.*, no. 1, pp. 31–34, 2013, doi: 10.1109/MWSYM.2013.6697492.
- [14] V. Teppati, M. Goano, A. Ferrero, V. Niculae, A. Olivieri, and G. Ghione, “Broad-band coaxial directional couplers for high-power applications,” *IEEE Trans. Microw. Theory Tech.*, vol. 51, no. 3, pp. 994–997, 2003, doi: 10.1109/TMTT.2003.808733.
- [15] V. Teppati, M. Goano, and A. Ferrero, “Conformal-mapping design tools for coaxial couplers with complex cross section,” *IEEE Trans. Microw. Theory Tech.*, vol. 50, no. 10, pp. 2339–2345, 2002, doi: 10.1109/TMTT.2002.803424.
- [16] H. J. Riblet and T. S. Saad, “A New Type of Waveguide Directional Coupler,” *Proc. IRE*, vol. 36, no. 1, pp. 61–64, 1948, doi: 10.1109/JRPROC.1948.230916.
- [17] S. Rosen and J. T. Bangert, “A Consideration of Directivity in Waveguide

- Directional Couplers,” *Proc. IRE*, vol. 37, no. 4, pp. 393–401, 1949, doi: 10.1109/JRPROC.1949.231964.
- [18] P. Kant, K. Dobrzyniewicz, and J. J. Michalski, “High Power Directional Coupler with Equal Tunable Coupling Value at 352 MHz and 704 MHz,” *IEEE MTT-S Int. Microw. Symp. Dig.*, vol. 2018-June, pp. 522–524, 2018, doi: 10.1109/MWSYM.2018.8439286.
- [19] S. M. Sohn, A. Gopinath, and J. T. Vaughan, “A Compact, High Power Capable, and Tunable High Directivity Microstrip Coupler,” *IEEE Trans. Microw. Theory Tech.*, vol. 64, no. 10, pp. 3217–3223, 2016, doi: 10.1109/TMTT.2016.2602835.
- [20] K. K. M. Cheng and S. Yeung, “A novel rat-race coupler with tunable power dividing ratio, ideal port isolation, and return loss performance,” *IEEE Trans. Microw. Theory Tech.*, vol. 61, no. 1, pp. 55–60, 2013, doi: 10.1109/TMTT.2012.2228219.
- [21] X. Tan, J. Sun, and F. Lin, “A Compact Frequency-Reconfigurable Rat-Race Coupler,” *IEEE Microw. Wirel. Components Lett.*, vol. 30, no. 7, pp. 665–668, 2020, doi: 10.1109/LMWC.2020.2993369.
- [22] Y. F. Pan, S. Y. Zheng, W. S. Chan, and H. W. Liu, “Compact Phase-Reconfigurable Couplers With Wide Tuning Range,” *IEEE Trans. Microw. Theory Tech.*, vol. 68, no. 2, pp. 681–692, 2020, doi: 10.1109/TMTT.2019.2950001.
- [23] H. N. Chu and T.-G. Ma, “Tunable Directional Coupler With Very Wide Tuning Range of Power Division Ratio,” *IEEE Microw. Wirel. Components Lett.*, vol. 29, no. 10, pp. 652–654, 2019, doi: 10.1109/LMWC.2019.2936317.
- [24] B. W. Xu, S. Y. Zheng, W. M. Wang, Y. Le Wu, and Y. A. Liu, “A Coupled Line-Based Coupler With Simultaneously Tunable Phase and Frequency,” *IEEE Trans. Circuits Syst. I Regul. Pap.*, vol. 66, no. 12, pp. 4637–4647, 2019, doi: 10.1109/TCSI.2019.2939931.
- [25] S. B. Cohn and R. Levy, “History of Microwave Passive Components with

- Particular Attention to Directional Couplers,” *IEEE Trans. Microw. Theory Tech.*, vol. 32, no. 9, pp. 1046–1054, 1984, doi: 10.1109/TMTT.1984.1132816.
- [26] W. W. Mumford, “Directional Couplers,” *Proc. IRE*, vol. 35, no. 2, pp. 160–165, 1947, doi: 10.1109/JRPROC.1947.231592.
- [27] H. C. Early, “A Wide-Band Directional Coupler for Wave Guide,” *Proc. IRE*, vol. 34, no. 11, pp. 883–886, 1946, doi: 10.1109/JRPROC.1946.232587.
- [28] H. J. Riblet, “The Short-Slot Hybrid Junction,” *Proc. IRE*, vol. 40, no. 2, pp. 180–184, 1952, doi: 10.1109/JRPROC.1952.274021.
- [29] J. Lange, “Interdigitated Stripline Quadrature Hybrid (Correspondence),” *IEEE Trans. Microw. Theory Tech.*, vol. 17, no. 12, pp. 1150–1151, 1969, doi: 10.1109/TMTT.1969.1127115.
- [30] A. Podell, “A High Directivity Microstrip Coupler Technique,” in *G-MTT 1970 International Microwave Symposium*, 1970, pp. 33–36, doi: 10.1109/GMTT.1970.1122761.
- [31] C.-S. Kim, C.-S. Yoon, J.-S. Park, D. Ahn, J.-B. Lim, and S.-I. Yang, “A design of the novel varactor tuned directional coupler,” in *1999 IEEE MTT-S International Microwave Symposium Digest (Cat. No.99CH36282)*, 1999, vol. 4, pp. 1725–1728 vol.4, doi: 10.1109/MWSYM.1999.780304.
- [32] S. M. Wang, C. Y. Chang, and J. Lin, “A software configurable coupler with programmable coupling coefficient,” *IEEE MTT-S Int. Microw. Symp. Dig.*, pp. 185–188, 2007, doi: 10.1109/MWSYM.2007.380321.
- [33] B. Arigong, M. Zhou, H. Ren, C. Chen, and H. Zhang, “A Compact Lumped-Component Coupler with Tunable Coupling Ratios and Reconfigurable Responses,” *IEEE MTT-S Int. Microw. Symp. Dig.*, vol. 2018-June, pp. 518–521, 2018, doi: 10.1109/MWSYM.2018.8439297.
- [34] H. Zhu and A. M. Abbosh, “A Compact Tunable Directional Coupler with Continuously Tuned Differential Phase,” *IEEE Microw. Wirel. Components Lett.*, vol. 28, no. 1, pp. 19–21, 2018, doi: 10.1109/LMWC.2017.2779819.

- [35] C. Errando-Herranz, M. Colangelo, S. Ahmed, J. Bjork, and K. B. Gylfason, “MEMS tunable silicon photonic grating coupler for post-assembly optimization of fiber-to-chip coupling,” *Proc. IEEE Int. Conf. Micro Electro Mech. Syst.*, pp. 293–296, 2017, doi: 10.1109/MEMSYS.2017.7863399.
- [36] H. Liu, S. Fang, and Z. Wang, “A Compact Trans-Directional Coupler with Wide Frequency Tuning Range and Superior Performance,” *IEEE Trans. Components, Packag. Manuf. Technol.*, vol. 7, no. 10, pp. 1670–1677, 2017, doi: 10.1109/TCPMT.2017.2692269.
- [37] Y. Yang, Z. Hou, X. Zhu, W. Che, and Q. Xue, “A Millimeter-Wave Reconfigurable On-Chip Coupler with Tunable Power-Dividing Ratios,” *2019 IEEE MTT-S Int. Wirel. Symp. IWS 2019 - Proc.*, vol. 67, no. 5, pp. 1516–1526, 2019, doi: 10.1109/IEEE-IWS.2019.8803950.
- [38] M. C. J. Chik and K. K. M. Cheng, “Group delay investigation of rat-race coupler design with tunable power dividing ratio,” *IEEE Microw. Wirel. Components Lett.*, vol. 24, no. 5, pp. 324–326, 2014, doi: 10.1109/LMWC.2014.2309085.
- [39] D. M. Pozar, *Microwave engineering; 3rd ed.* Hoboken, NJ: Wiley, 2005.
- [41] L. De Lange and D. J. Ludick, “Application of Machine Learning for Antenna Array Failure Analysis,” *CEMi 2018 - Int. Work. Comput. Electromagn. Mach. Intell.*, pp. 5–6, 2019, doi: 10.1109/CEMI.2018.8610651.
- [42] J. Persano, S. Mikki, and Y. M. M. Antar, “A novel massively-parallel processing framework for real-time MIMO and smart antenna array beam control,” *CEM 2017 - 2017 Comput. Electromagn. Int. Work.*, pp. 11–12, 2017, doi: 10.1109/CEM.2017.7991862.
- [43] C. G. Christodoulou, J. A. Rohwer, and C. T. Abdallah, “The use of machine learning in smart antennas,” *IEEE Antennas Propag. Soc. AP-S Int. Symp.*, vol. 1, pp. 321–324, 2004, doi: 10.1109/aps.2004.1329637.
- [44] N. Xu, C. G. Christodoulou, M. Martinez-Ramon, and T. Özdemir, “Antenna array processing for radar applications using support vector machines,” *IEEE*

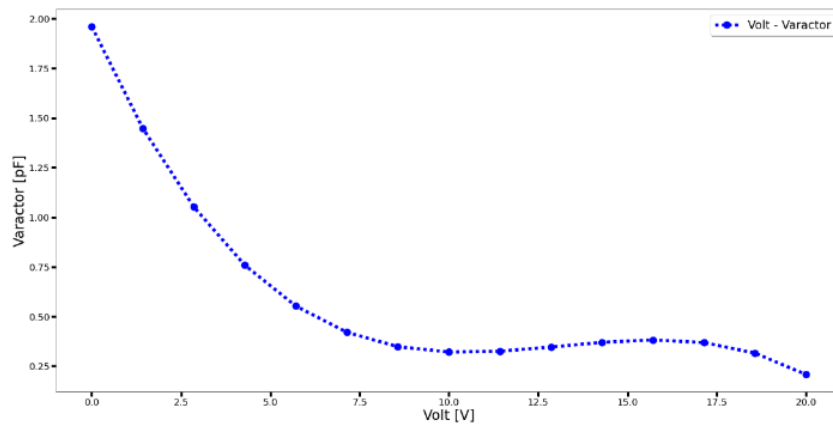
- Antennas Propag. Soc. AP-S Int. Symp.*, pp. 1295–1298, 2006, doi: 10.1109/APS.2006.1710781.
- [45] F. Willnecker, I. Anantavraslip, and B. Brügge, “Machine learning assisted position detection of UHF RFID tags,” *Smart SysTech 2012 - Eur. Conf. Smart Objects, Syst. Technol.*, 2012.
- [46] J. Tak, A. Kantemur, Y. Sharma, and H. Xin, “A 3-D-printed W-band slotted waveguide array antenna optimized using machine learning,” *IEEE Antennas Wirel. Propag. Lett.*, vol. 17, no. 11, pp. 2008–2012, 2018, doi: 10.1109/LAWP.2018.2857807.
- [47] Q. Wu, H. Wang, and W. Hong, “Broadband Millimeter-Wave SIW Cavity-Backed Slot Antenna for 5G Applications Using Machine-Learning-Assisted Optimization Method,” *2019 Int. Work. Antenna Technol. iWAT 2019*, pp. 9–12, 2019, doi: 10.1109/IWAT.2019.8730801.
- [48] N. Xu, C. G. Christodoulou, S. E. Barbin, and M. Martínez-Ramón, “Detecting failure of antenna array elements using machine learning optimization,” *IEEE Antennas Propag. Soc. AP-S Int. Symp.*, vol. 87131, no. 1, pp. 5753–5756, 2007, doi: 10.1109/APS.2007.4396858.
- [49] X. Wang, P. Wang, and X. Wang, “Adaptive Sparse Array Reconfiguration based on Machine Learning Algorithms,” *ICASSP, IEEE Int. Conf. Acoust. Speech Signal Process. - Proc.*, vol. 2018-April, pp. 1159–1163, 2018, doi: 10.1109/ICASSP.2018.8461429.
- [50] R. R. Alavi, R. Mirzavand, J. Doucette, and P. Mousavi, “An Adaptive Data Acquisition and Clustering Technique to Enhance the Speed of Spherical Near-Field Antenna Measurements,” *IEEE Antennas Wirel. Propag. Lett.*, vol. 18, no. 11, pp. 2325–2329, 2019, doi: 10.1109/LAWP.2019.2938732.

Appendices

Appendix A

Varactor Diode Value

Varactor diode has been selected from Skyworks Solutions Inc. (SVM2019). Varactor value is shown in Appendix Figure 1 with changing reverse bias voltage value. The varactors are subjected to a reverse voltage ranging from 0 to 20 V, causing the capacitance to fluctuate between 2.2 and 0.3 pF.



Appendix Figure 1: Biasing reverse voltage (V) & varactor value (pF)

Appendix B

Validation of Regression Machine Learning Problem

Three metrics are commonly used for assessing predictions on regression problems. These are Mean Squared Error (MSE), Root Mean Squared Error, and R-Squared Error.

MSE is the average of the squared difference between the data set's original and predicted values. MSE measures the performance of a machine learning model, estimator, it is always positive and it can be said that estimators with MSE value close to zero perform better.

The root mean square error (RMSE) is the residuals' standard deviation. Residuals are a measure of how distant the data points are from the regression line; RMSE is a measure of how to spread out these residuals are. In other words, it indicates how tightly the data is clustered around the line of best fit.

$$MSE = \frac{1}{n} \sum_{i=1}^n (y_i - \hat{y})^2 \quad (\text{Appendix.1})$$

$$RMSE = \sqrt{\frac{1}{n} \sum_{i=1}^n (y_i - \hat{y})^2} \quad (\text{Appendix.2})$$

Where,

\hat{y} - predicted value of y

The R2 statistic indicates how well a set of predictions fits the actual data. The coefficient of determination is the phrase used in statistical literature to describe this

metric. This is a number between 0 and 1 that represents a no-fit or perfect-fit situation. With a value near zero and less than 0.5, the predictions show a poor match to the actual data.

$$R^2 = 1 - \frac{\sum(y_i - \hat{y})^2}{\sum(y_i - \bar{y})^2} \quad (\text{Appendix.3})$$

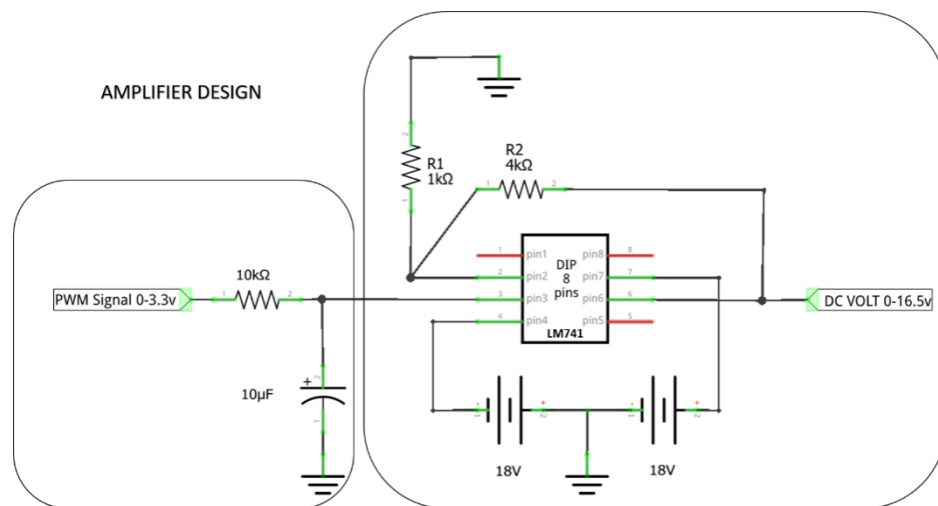
Where,

\bar{y} - mean value of y

Appendix C

Amplifier Schematics

As shown from Appendix Figure 2 in the amplifier schematic diagram, the amplifier circuit may be built using only three resistor, one capacitor, two battery and LM741 opamp.



Appendix Figure 2: The amplifier schematics

The circuits take a tiny signal as an input and output the amplified signal. The two resistors R1 and R2 regulate the gain according to this simple law:

$$\text{Gain} = (1+R2/R1) \quad (6.1)$$

This circuit above provides a gain of about 5 when R2 and R1 are selected 4kΩ and 1kΩ, respectively. This means the voltage output will be 5 times greater than the voltage input. So, the maximum 3.3 Volt PWM signal that DAC converts to analog signal is increased by 5 times to 16.5 DC Volt.

Republic of Turkey
İzmir Kâtip Çelebi University
Graduate School of Natural and Applied Sciences

Electronic Controlled Vertical Integration Directional Coupler Design with Artificial Neural Networks for Dual Band Application

Department of Electrical and Electronics in Engineering
Master's Thesis

Hacer DANACI
ORCID 0000-0003-4057-4749

Thesis Advisor: Assoc. Prof. Dr. Merih PALANDÖKEN

September 2021

DANACI E. C. V. I. D. Coupler D. A. N. N. D. B. A. MASTER'S THESIS 2021

Curriculum Vitae

Name Surname : Hacer Danacı
E-mail (1) : Y180207005 @ikcu.edu.tr
E-mail (2) : haker.danaci.muh@gmail.com

Education:

2011–2016 Ege University, Department of Electrical and Electronics in Engineering

2019–2021 İzmir Kâtip Çelebi University, Graduate School of Natural and Applied Sciences, Department of Electrical and Electronics in Engineering

Work Experience:

2015 – 2016 Türk Telekom Intern
2017 – 2018 Duru Yapı Denetim Electrical and Electronics Engineer
2019 – 2020 İzmir Kâtip Çelebi University BAP Bursary
2020 – 2021 Harp Arge A. Ş. Electrical and Electronics Engineer

Publications (if any):

1. Danacı, H. Palandöken, M. (2020). A Novel Electronically Reconfigurable Antenna Design for RFID and GSM 900 MHz Applications Avrupa Bilim ve Teknoloji Dergisi, Ejosat Special Issue 2020 (ICCEES), 304-307. DOI: 10.31590/ejosat.804511
2. Danacı, H. Oner, A. M. Palandöken, M. Optimization of the Directional Coupler with Machine Learning for 900 MHz GSM Band Application. 2nd International Eurasian Conference on Science, Engineering and Technology. 2020.
3. Danacı, H. Gerek, B. Palandöken, M. A novel Electronically Tunable Phase Shifter Design for GLONASS Frequency Band Applications. 2nd International Eurasian Conference on Science, Engineering and Technology. 2020.